Dynamics of episodic magma injection and migration at Yellowstone caldera: revisiting the 2004-2009 episode of caldera uplift with InSAR and GPS data

Francisco Delgado, Raphaël Grandin

[1]Université de Paris, Institut de Physique du Globe de Paris, CNRS, F-75005 Paris, France

Key Points:

- We reanalyze all the ENVISAT InSAR and GPS data that span the 2004-2009 episode of unrest
- The GPS and InSAR time series record uplift with an exponential increase followed by an exponential decrease
- Magma injection is the driving mechanism of unrest with no need to invoke exsolved volatiles

Corresponding author: Francisco Delgado, `delgado@ipgp.fr`

Abstract

The 2004-2009 uplift episode is the largest recorded episode of unrest at Yellowstone caldera. We use GPS and InSAR time series spanning 2004-2015, with a focus in the aforementioned event to understand the mechanisms of unrest. InSAR data recorded $\sim$25 and $\sim$20 cm of uplift at the Sour Creek (SCD) and Mallard Lake (MLD) resurgent domes during 2004-2009, and $\sim$8 cm of subsidence at the Norris Geyser Basin (NGB). The SCD/MLD uplift was followed by subsidence across the caldera floor with a maximum at MLD of $\sim$1.5-2.5 cm/yr and no deformation at NGB. The best-fit source models are two horizontal sills at depths of $\sim$8.7 and 10.7 km for the caldera source and NGB respectively, with volume changes of 0.354 and -0.121 km^3, and an overpressure of $\sim$0.1 MPa. The InSAR and GPS time series record an exponential increase followed by exponential decrease in the uplift, which is indicative of magma injection into the caldera reservoir, with no need for other mechanisms. However, magma extraction from NGB to the caldera is unable to explain the subsidence coeval with the caldera uplift. The GPS time series of the 2014-2015 episode of caldera uplift can also be explained by a magma injection model.Distributed sill opening models show that magma is stored across the caldera source with no clear boundary between MLD and SCD. Since the magma overpressure is orders below the tensile strength of the encasing rock, historical episodes of unrest like these are very unlikely to trigger an eruption.

1 Introduction

Silicic volcanoes ($SiO_2 > 69\%$) are responsible for the largest explosive eruptions on Earth (VEI > 8, (*Miller and Wark*, 2008; *Bachmann and Bergantz*, 2008)), more than two orders of magnitude larger than any eruption with recorded visual and instrumental observations. These eruptions form calderas that can remain restless even several hundreds of thousands of years after the climactic eruptions (e.g., (*Hill et al.*, 2020)). Several of these calderas undergo transient pulses or cycles of ground uplift followed by periods of either quiescence or ground subsidence ((*Pelton and Smith*, 1979; *Dvorak and Berrino*, 1991)). However, their relation to potential eruptive activity has remained elusive (e.g., (*Pritchard et al.*, 2019)). The advent of interferometric synthetic aperture radar (InSAR) geodesy in the early 1990s provided the first detailed images of the spatial and temporal complexities of these ground deformation cycles ((*Wicks et al.*, 1998; *Lundgren et al.*, 2001)), which have been imaged at Yellowstone ((*Wicks et al.*, 1998, 2006; *Chang et al.*, 2007,0)), Long Valley ((*Fialko et al.*, 2001a; *Liu et al.*, 2011; *Montgomery-Brown et al.*, 2015)), Campi Flegrei ((*Lundgren et al.*, 2001; *Trasatti et al.*, 2015; *D'Auria et al.*, 2015)) Santorini ((*Parks et al.*, 2012)), Laguna del Maule ((*Feigl et al.*, 2014; *Le Mével et al.*, 2015)) and Cordón Caulle ((*Jay et al.*, 2014; *Delgado et al.*, 2016,0)) volcanoes. These uplift events have velocities of $\sim$1-10 cm/yr, but can reach fast rates up to 28 - 45 cm/yr ((*Feigl et al.*, 2014; *Delgado et al.*, 2016)). The spatial and time scales of the deformation events vary from $\sim$15 km in Long Valley to more than 70 km at Yellowstone, and from $\sim$6 months for Cordon Caulle ((*Delgado et al.*, 2018)) up to at least half a century for Yellowstone ((*Pelton and Smith*, 1979)). These signals have been interpreted as being produced by either magma injection in shallow reservoirs ((*Wicks et al.*, 2006; *Delgado et al.*, 2018; *Miller et al.*, 2017)), volatile exsolution ((*Dzurisin et al.*, 2012; *Hildreth*, 2017)), fluid flow in the hydrothermal systems that are located in several of these systems ((*Hurwitz et al.*, 2007a)) or a combination of these processes ((*Dzurisin et al.*, 2012; *Tizzani et al.*, 2015)). However, inherent ambiguities in the interpretation of the geodetic data and the lack of other constraining independent data sets like microgravity, gas chemistry, seismology and heat flow measurements have precluded to unravel the geological mechanism of ground uplift for most of them. Despite the diversity of monitoring data acquired in the past 40 years, recent studies that try to reconcile the wealth of geologic and geophysical data of Long Valley ((*Hildreth*, 2017; *Hill et al.*, 2020)) and Campi

Flegrei ((*Troise et al.*, 2019), (*D'Auria et al.*, 2015)) calderas show no agreement upon the driving mechanism of unrest.

The understanding of these unrest signals require a thorough knowledge of the processes that occur inside these magma reservoirs. For instance, all the models available for modeling ground deformation data assume injection of fluid magma with Newtonian viscosity into a pressurized cavity ((*Lengline et al.*, 2008; *Le Mével et al.*, 2016)). This is in contrast with the current understanding of the plumbing system of silicic volcanoes as crystal mushes, in which reservoirs are not molten but solid sponge-like bodies with pores filled with interstitial fluids and melt ((*Bachmann and Bergantz*, 2008; *Bachmann and Huber*, 2016; *Cashman et al.*, 2017; *Cooper*, 2017)). These mushes have a protracted grow history by episodic amalgamation of a stack of sill-shaped reservoirs, in agreement with numerical simulations ((*Annen*, 2009; *Annen et al.*, 2015)), and spend most of their lifetime below their solidus under cold storage conditions ((*Cooper and Kent*, 2014; *Rubin et al.*, 2017)). Crystal mushes are unlikely to produce a volcanic eruption unless they are thermomecanically unlocked and remobilized by many episodic pulses of magma injection ((*Huber et al.*, 2010,0)). However, thermomechanical remobilization is important only over long time scales of 10^2-10^3 years, while on short time scales of 10^0-10^1 years magma injection is the principal triggering mechanism of rhyolitic eruptions ((*Huber et al.*, 2011,0; *Degruyter and Huber*, 2014; *Townsend et al.*, 2019)). Other views indicate that unrest on time scales of 10^0-10^1 years at large silicic systems may also be explained by melt amalgamation resulting from the inherent instability of buoyant melt layers ((*Sparks et al.*, 2019)). On the other hand, views that consider non-magmatic processes suggest that caldera unrest results from a combination of magma injection, volatile exsolution and/or crystallization and degassing of large magma batches without new inputs of magma. Caldera uplift is then punctuated by episodic leaks of fluids from below the brittle-ductile transition (BDT) to shallow areas that deform in a brittle way ((*Fournier*, 2007)). Further, seismic and geodetic data show that episodes of uplift resulting from likely magma injections are transient features and can be separated by many years ((*Delgado et al.*, 2018; *Druitt et al.*, 2019)) or even decades ((*Sigmundsson et al.*, 2010; *Druitt et al.*, 2019)) without any other clear evidence for unrest. Other views suggest that caldera resurgence is the direct consequence of episodic magma injection resulting from the incremental and protracted growth of plumbing systems. The episodic uplift is interrupted by episodes of deflation but the net result is uplift ((*Acocella*, 2019)). Therefore, regardless of the the mechanism of unrest, it is a significant and key question in volcano science when do these pulses of uplift imply a potential eruption. as it has direct implications for models of hazard assessment (e.g., (*Pritchard et al.*, 2019)).

If these uplift events are in turn produced by magma injection, how many of them and of what magnitude are required to actually trigger an eruption? Unfortunately, the models used to study active intrusions ((*Lengline et al.*, 2008; *Le Mével et al.*, 2016)) do not have predictive capabilities and cannot predict the maximum stress in the reservoir walls produced by magma injection. This is a key element in eruption forecasting models because dikes that transport magma from the reservoir towards the surface form when the deviatoric hoop stress in the reservoir walls reaches a threshold above the tensile strength of the rock which is known to be within ∼1-40 MPa ((*Tait et al.*, 1989; *Albino et al.*, 2010)). Nonetheless, given our imperfect knowledge of the shallow reservoir location, size and physicochemical state, the exact rupture threshold is unknown. Furthermore, the maximum pressurization that reservoirs sustain before an eruption likely varies throughout the lifetime of a single edifice and between different volcanoes ((*Lu et al.*, 2003; *Pinel et al.*, 2010; *Carrier et al.*, 2015)).

In this study we focus on the episode of unrest during 2004-2009 at Yellowstone ((*Chang et al.*, 2007,0)), the fastest ever recorded at that volcano since systematic geodetic measurements started in 1975 ((*Pelton and Smith*, 1979)). Yellowstone caldera has been studied for more than two decades with InSAR and despite the good quality of the geodetic observations, previous studies have used limited amounts data – usually a few interferograms only (e.g., (*Wicks et al.*, 1998, 2006; *Chang et al.*, 2007; *Wicks et al.*, 2020)). Further, despite more than 4 decades of geodetic observations at Yellowstone, there is still significant uncertainty on the driving mechanisms of ground deformation ((*Dzurisin et al.*, 2012; *Hurwitz and Lowenstern*, 2014)). For example, a detailed conceptual model does not assess the relative contributions of basalt injections and exsolved volatiles ((*Dzurisin et al.*, 2012)). We test the hypothesis of whether the 2004-2009 episode of unrest was caused by magma injection or other mechanisms, and particularly the nature of the fluids involved in the episodes of unrest ((*Hurwitz et al.*, 2007a; *Dzurisin et al.*, 2012)). To assess these questions, we use all the continuous GPS and all the ENVISAT InSAR data that recorded the complete 2004-2009 episode of uplift with improved source models of ground deformation and solid-fluid mechanics models of magma injection. These models are function of the magma viscosity, magma compressibility and conduit radius among other parameters abd can predict the time series of ground deformation (e.g,m (*Lengline et al.*, 2008; *Le Mével et al.*, 2016; *Delgado et al.*, 2018)). We compare the deformation data and models with other seismic swarms in December 2008 ((*Farrell et al.*, 2010)) and January 2010 ((*Shelly et al.*, 2013)) and discuss mechanisms of transition from caldera uplift to subsidence. We finally extend our models to the most recent periods of unrest during 2014-2015 ((*Wicks et al.*, 2020))

2 Geological and ground deformation background of Yellowstone caldera

Yellowstone caldera is a $\sim$85$\times$45 km^3 topographic depression and is the youngest of three collapse calderas in the Yellowstone plateau. The eruptions that formed these calderas occurred 2.1, 1.3 and 0.64 Myrs ago erupting the Huckleberry Ridge, Mesa Falls and Lava Creek Tuffs with erupted volumes larger than 2450, 280 and 1000 km^3 respectively ((*Christiansen*, 2001)). The last of these eruptions formed the current Yellowstone caldera, which is now filled with 600-1000 km^3 of post caldera rhyolitic lava flows. Post caldera volcanism has been focused on the Sour Creek and Mallard Lake domes (SCD and MLD hereafter) (Figure 1) which have been active for the past 0.164 Myrs ((*Christiansen*, 2001)). The caldera is underlain by a large plumbing system with large but spatially variable contents of melt ((*Farrell et al.*, 2014; *Huang et al.*, 2015; *Schmandt et al.*, 2019)). Yellowstone hosts the largest hydrothermal system in the world with half of the world's geysers ((*Hurwitz and Manga*, 2017)) and several hundreds of hydrothermal vents ((*Fournier*, 1989; *Lowenstern and Hurwitz*, 2008; *Hurwitz and Lowenstern*, 2014)). On a geological time scale, the VEI 8 eruptions and the large hydrothermal activity are fuelled by large batches of basalt injection under the upper to mid-crustal silicic system, evidenced by a very large CO_2 degassing flux which requires that the injecting basaltic magma has a CO_2 concentration of 400-500 ppm. Such a large amount of CO_2 cannot be dissolved in silicic melts because it would be completely exhausted in 1000 years. Mass balances indicate that $\sim$0.3 km^3/yr of basaltic melts are intruded beneath the caldera, a similar amount to that intruded at the Hawaii hot spot ((*Lowenstern and Hurwitz*, 2008; *Lowenstern et al.*, 2015)). These injections are also the ultimate source of caldera unrest ((*Wicks et al.*, 2006; *Dzurisin et al.*, 2012)).

2.1 Observations and models of caldera unrest

A summary of geodetic observations of ground deformation between 1923 and 2008 is described in detail in (*Dzurisin et al.*, 2012). Ground deformation was observed for the first time in 1975 when leveling lines were measured after 1923 recording 0.7 m of uplift with a time-averaged rate of $\sim$1.4 cm/yr ((*Pelton and Smith*, 1979)). Systematic time-lapse leveling started in 1983 until 2007, and showed that the caldera floor uplifted until 1984 when the uplift shifted to subsidence following the largest historical swarm ever measured at Yellowstone with M_C magnitudes up to 4.9 ((*Waite and Smith*, 2002)). Caldera subsidence continued until 1996 when a 1 year long episode of caldera uplift was recorded ((*Wicks et al.*, 1998)). Coevally, the area of Norris Geyser Basin (NGB herefater) uplifted between 1996 and 2000 ((*Wicks et al.*, 2006)). Continuous GPS monitoring started in 1996 with a five-fold increase in the station density in 2000 (Figure 1). In July 2004, the whole caldera floor uplifted in the largest episode of historic unrest with a maximum uplift rate of 7 cm/yr and with subsidence at rates of 2 cm/yr at NGB ((*Chang et al.*, 2007,0)). The caldera uplift ended in mid 2009, coevally with another seismic swarm in the NW part of the caldera (*Shelly et al.* (2013)). More recent episodes of unrest include uplift at NGB between December 2013 and March 30 2014, subsidence at NGB and uplift at the caldera between March 2014 and early 2015, and NGB uplift and caldera subsidence since then ((*Dzurisin et al.*, 2019; *Wicks et al.*, 2020)) (Figure 1). The transition from uplift to subsidence usually occurs with large seismic swarms at the distal parts of the caldera ((*Waite and Smith*, 2002; *Shelly et al.*, 2013)).

Previous InSAR studies have focused in ERS-1/2 data to measure caldera floor subsidence during 1992 to 1995, slight caldera floor uplift during 1995-1996 and uplift at NGB during 1996-2000 ((*Wicks et al.*, 1998, 2006; *Dzurisin et al.*, 1999; *Dzurisin and Lu*, 2007; *Dzurisin et al.*, 2012,0; *Vasco et al.*, 2007; *Aly and Cochran*, 2011; *Tizzani et al.*, 2015; *Wicks et al.*, 2020)), caldera uplift with ENVISAT during 2004-2009 ((*Chang et al.*, 2007,0; *Aly and Cochran*, 2011; *Dzurisin et al.*, 2012; *Tizzani et al.*, 2015)), and NGB uplift, subsidence and then uplift with TerraSAR-X and Sentinel-1 data during December 2013 - March 2014, March 2014 - early 2015 and then 2016 - 2017 respectively ((*Dzurisin et al.*, 2019; *Wicks et al.*, 2020)). Despite the good quality of the InSAR observations, all the previous studies have used small amounts of data that provide individual snapshots of the individual episodes of unrest. The only exception is (*Tizzani et al.*, 2015) who calculated an InSAR time series with a descending ERS/ENVISAT track for 1992-2010.

3 Deformation results

We use GPS data from five stations that record the complete sequence of uplift and subsidence during 2004-2009 (Figure 1), operated by the University of Utah and the EarthScope Plate Boundary Observatory (Figure 1, Figure S1). The data were processed by the Nevada Geodetic Laboratory. We use InSAR data from the C-band ERS-1/2, ENVISAT, L-band ALOS and X-band TerraSAR-X satellites (Table 1) processed and analyzed with a variety of methods depending upon the satellite platform, and data temporal resolution (Figure 2 - Figure 3, Figures S2-S3). Data processing follows standard procedures for time series analysis (e.g., (*Doin et al.*, 2011)) and is described in detail in the supplementary material. From the InSAR time series we calculate cumulative total ground deformation during the episode of uplift as the difference in deformation between the last image in 2009 and the first image in 2004 or 2005. These data span the complete episode of caldera uplift and are hereafter referred as interferograms.

Despite the different amount of SAR images and the variable interferogram quality of the data in the different ENVISAT tracks, each of the time series record a total of ~25 and ~20 cm of line-of-sight (LOS) uplift at SCD and MLD between September 2004 and September 2009 (Figure 2 - Figure 3). The InSAR data also record ~8 cm of subsidence at the NGB between 2004 and 2008 – one year before the end of the uplift at the resurgent domes (Figure 3). However, the onset of deformation at SCD, MLD and NGB cannot be assessed from the InSAR data because there are only two non-winter images in 2004. The wavelength of the deformation signals at SCD, MLD and NGB is constant during 2004-2009 and does not change during the recorded time span, indicating deformation sources that do not change their depth (not shown). The GPS stations OFW2 located near the MLD and HVWY, LKWY and WLWY located near the SCD record between ~10 and 20 cm of uplift during the same time span, in agreement with them being at variable distances from the areas of maximum uplift (Figure 1). The deformation signals are similar in location and wavelength than those analyzed in previous studies ((*Chang et al.*, 2007,0; *Aly and Cochran*, 2011; *Tizzani et al.*, 2015; *Wicks et al.*, 2020)). A seismic swarm that occurred in December 2008 and detected by the LKWY station ((*Farrell et al.*, 2010)) is not observed by the InSAR data because we do not include winter images and because the geodetic signals it produced are below the InSAR uncertainty. The caldera uplift transitioned to subsidence in early 2010 until late 2013. The GPS data recorded this with a constant rate of ~1.5 cm/yr, but only the ENVISAT IM2 descending data recorded it (Figure 2C), with an average subsidence of 1-2 cm. ALOS-1 interferograms display double-bounce signals in wetlands that introduce abrupt phase discontinuities (e.g., (*Wdowinski and Hong*, 2015)) and phase unwrapping errors that cannot be corrected. Visual analysis of this data set shows no deformation during 2010-2011, so the data are not considered further in this study. The TSX data record no deformation at NGB, and the maximum caldera subsidence at MLD instead of SCD, with a maximum of -3.5 to -2 cm/yr depending on the track and on the amount of data used in the stacks. The deformation pattern of the 2011-2013 subsidence is significantly different to that of the 2004-2009 uplift. No clear evidence of localized fault creep triggered by magmatic deformation was observed on any of the InSAR time series. Both the GPS data for stations OFW2, HVWY, LKWY and WLWY and InSAR time series during 2004-2009 display a pattern of uplift in which deformation increases exponentially until a threshold is reached and followed by an exponential decrease (Figure 7). This exponential increase followed by exponential decrease is referred hereafter as double exponential ((*Le Mével et al.*, 2015)).

4 Source modeling

To understand the sources responsible for the ground deformation at Yellowstone, we jointly invert the interferograms and the GPS vectors with two sources. These include a tensile dislocation ((*Okada*, 1985)) representing an opening sill below the caldera floor plus an additional source to model the deflation below the NGB – either a pressurized small sphere (*McTigue* (1987)) or another tensile dislocation. We do not invert the 2010-2012 deformation data because the TSX data show velocity differences up to ~50% with respect to the GPS data. The wavelength of the deformation signals are of several tens of kilometers, suggesting that the deformation sources are likely to lie below the BDT. However, (*Tizzani et al.*, 2015) has shown that viscoelastic effects representative of viscous rheologies are only relevant for time scales longer than 580 years which are well below the time span of one decade considered in this study.

Prior to source modeling, linear ramps were estimated in areas with no deformation and removed from the interferograms. The data were then downsampled with a resolution-based algorithm ((*Lohman and Simons*, 2005)) with a sill geometry at a depth of 15 km. This source is only used to focus the downsampling in areas with deformation and not to enforce an a priori source model (Figure 4, S6). Downsampling with a shallower sill does not result in a vastly different number of downsampled patches. We use a diagonal data covariance matrix for the InSAR data because the data have a very weak spatial correlation no bigger than a few downsampled pixels and because the far-field variance in non-deforming areas is ~7 mm. Both GPS and InSAR data were weighted by the inverse of their uncertainties. Data were inverted with the neighborhood algorithm ((*Sambridge*, 1999)), a non-linear inversion method which iteratively searches for the best-fit model parameters avoiding local minima. Due to the vastly different amount of GPS and InSAR data points – 10 vs ~2500 points, the

GPS data should be weighted such that the InSAR data will not dominate the best-fit model. Hence, the GPS data were weighted with factors of 1, 0.2 and 0.1 to augment the relative weight of this data set with respect to InSAR and to test the optimal weighting for a joint inversions (e.g., (*Fialko*, 2004)). Inversions with these weighting factors result in models that do not significantly differ from each other, fitting equally well both GPS and InSAR data. Hence, both data sets are assigned equal weights in the non-linear inversion.

The model of a horizontal sill below the caldera floor and a depressurized sphere below NGB does not produce a fit as nearly as good compared to that of two dislocations. Therefore we focus on a model of two Okada sills onlys. After convergence was reached by the NA inversion resulting in models that do not significantly differ from each other, we use the Levenberg-Marquardt (LM) algorithm using the NA inversion model as the initial point of this inversion to find the global best-fit model. Inversions for all 14 non-linear model parameters (X and Y sill centroid, depth, strike, dip, width, length) for the two sub horizontal dislocations provide good data fits but fail to converge to a stable family of solutions because the sources lie on top of each other and thereby they strongly trade-off. After several iterations we fix the dip and strike of the caldera source to 0 and 54 because they converge rapidly to these values. Inversions for the rest of the 12 model parameters converge for the caldera source but not for the NGB source. We discard models in which the NGB and the caldera sills intersect with each other and since the NGB source dip is close to zero, we fix this model parameter to 0. Since convergence was reached for the caldera source parameters, we fix them and then invert for the NGB source, similar to other studies where the deformation signals of different sources interfere with each other (e.g., (*Bagnardi et al.*, 2013)). The best-fit geometry is made up of two horizontal sills (Figure 4, Table 2) at depths of 8.7 and 10.6 km for the caldera and the NGB sources respectively (Figure S5). Because we iteratively fixed the model parameters to ensure inversion convergence, it is neither feasible nor meaningful to calculate model parameter uncertainties. To ensure that the model is robust, we also inverted the data with a different algorithm based on a non-linear least square iterative inversion ((*Tarantola and Valette*, 1982)) retrieving very similar results. The vertical components of the five GPS stations were inverted for the caldera sill opening and NGB sill closing for every epoch to retrieve the cumulative volume change of the uniform opening model (Figure 6).

The Okada model does not include the pressure change as a model parameter so we follow two approaches to estimate it. First, the area of the caldera source sill ($\sim 58 \times 19$ km^2) can be roughly approximated by that of three penny-shaped cracks with a radii $a = 9.7$ km for each one, and we use the formula $\Delta V = \frac{8}{3}a^3(1-\nu)\frac{\Delta P}{G}$ ((*Fialko et al.*, 2001b)) to get an order of magnitude of the sill pressure change. This approach is just a very coarse approximation and does not imply that an Okada volume change is directly comparable to that of a pressurized penny-shaped crack. Using a volume change of $\Delta V \sim \frac{0.35}{3}$ km^3 for each of these sources and a shear modulus of 2.1 GPa ((*Heap et al.*, 2020)) we get a source overpressure of 0.13 MPa. Second, we fix the caldera sill centroid and dimensions and invert the InSAR data with the DEFVOLC mixed boundary element model (MBEM) (((*Cayol and Cornet*, 1997)) to calculate the source pressure changes produced by a pressurized ellipsoidal crack and a pressurized quadrangle source with a shear modulus of 2.1 GPa ((*Heap et al.*, 2020)). We only invert the IM2 interferogram because it is the most coherent data, several parameters are fixed and to increase the inversion speed. The boundary element model predicts sources at depths of 17 and 13 km respectively and a pressure change of ~0.08 MPa, %60 than the value inferred from the crack approximation.These sources are much deeper than those inferred from the inversion of the Okada models. The ovepressure for both models are several orders of magnitude below the tensile strength of the encasing rocks of 10-40 MPa (e.g., *Albino et al.* (2010); **?**).

The inversion for dislocations with uniform opening results in non-negligible residuals near MLD and SCD (Figure S5), which potentially result from localized areas of fluid pressurization below the resurgent domes. To improve the data fit, we use a distributed sill-opening model for the caldera sill (e.g., (*Delgado et al.*, 2018; *Henderson et al.*, 2017)), in which the best-fit sill is augmented to 12×8 smaller 5×5 km^2 sills and with the constrain that the sill opening tapers to zero in its edges (Figure 4, Figures S6-S7). The model is regularized with Laplacian smoothing to avoid unrealistic oscillatory opening and the amount of smoothing is chosen by the "L curve" corner ((*Aster et al.*, 2018)). We jointly invert GPS and InSAR data with weighting factors α_W between 1 (equal weight for GPS and InSAR), 0.5 and 0.2 to augment the GPS contribution with respect to InSAR. The model fit to the GPS data improves with $\alpha_W = 0.5$ at the expense of a worst data fit to the InSAR data near NGB. Smaller α_W result in a near complete fit to the GPS data but higher residuals for the InSAR data. Therefore, we invert the data with $\alpha_W = 0.5$ which provides good data fits without increasing significantly the residual for the NGB signal recorded by the interferograms. The distributed opening model predicts volume changes for the caldera source of 0.354 km^3 during 2004-2009 – a time averaged value of 0.07 km^3/yr, 0.306 km^3 during 2005-2009 and a volume decrease for the NGB source of -0.121 km^3 and -0.0981 km^3 for the same time periods respectively. The distributed opening models show no clear boundary between the zones of volume change beneath SCD and MLD (Figure 5). A residual of ∼5 cm is observed in the E part of Yellowstone Lake particularly in the ascending interferograms and could be related to the ecember 2008 seismic swarm ((*Farrell et al.*, 2010)).

5 Dynamic model of magma injection and transport

Kinematic source models like the aforementioned two sills do not provide insights on the physical mechanism driving the caldera uplift. In this study we focus solely on the mechanism of magma injection from a deep source to a shallow source because there are simple analytic formulas that can be compared directly with ground deformation time series ((*Lengline et al.*, 2008; *Le Mével et al.*, 2016)). Hereafter we refer to magma as molten rock with a Newtonian viscosity. Although the reviews of (*Dzurisin et al.*, 2012) and (*Lowenstern et al.*, 2015) suggest the role of both hydrothermal and magmatic fluids, including exsolved volatiles from cooling magma, in this study we neglect theses effects. This is a clear oversimplification of the very complex hydrothermal-magmatic system of Yellowstone, but it allows to tests to what extent ground deformation can be explained by one of these end-member models.

We start with a magma injection model in which the caldera reservoir is connected to a magma source in the mantle, whose source pressure function increases linearly until a threshold value when it reaches a constant. Magma ascends due to its overpressure and pressurizes the shallow reservoir, resulting in a double exponential function for both the reservoir overpressure and the ground displacement ((*Le Mével et al.*, 2016)). In the case of Yellowstone, this model does not take into account the potential connection between NGB and the caldera source, which is addressed later in the study. The magma injection model is defined by Equation 1- Equation 2.

$$P(t) = \begin{cases} \frac{st}{t^*} + (s\tau_p - \Delta\rho g L)(e^{\frac{-t}{\tau_p}} - 1) & 0 < t < t^* \\ st(\frac{\tau_p}{t^*} e^{\frac{-t}{\tau_p}} - \frac{\tau_p}{t^*} e^{\frac{-(t-t^*)}{\tau_p}} + 1) & t > t^* \end{cases} \tag{1}$$

$$\tau_p = \frac{8\eta L V(\beta_w + \beta_m)}{\pi R^4} \tag{2}$$

Here t^* is the transition time between linear increasing and constant deep pressurization, τ_p is a constant that depends on the properties of the plumbing system, R

is the conduit radius, L is the conduit length, V is the reservoir volume, β_w and β_m are the reservoir and magma compressibility and s is the pressurization rate. Since the source pressure is proportional to the displacement for pressurized cavities embedded in a linear-elastic half-space ((*McTigue*, 1987)), the model can be scaled with an arbitrary constant to model the GPS time series. This way, the constant scales displacement to pressure for models that do not include the source overpressure as a model parameter (e.g., (*Henderson et al.*, 2017)). Further, if no changes occur in the plumbing system like a change in the source geometry, transient changes in the time series are direct evidence of transient changes in the reservoir pressure and ultimately in the deep source pressure function. As stated earlier, the InSAR data does not show changes in the wavelength of the deformation signals so the sources are fixed in depth. This way we discard that changes in the time series results from changes in the source geometry.

The vertical components of the WLWY, LKWY and OFW2 stations are almost insensitive to the opening of the NGB sill (Figure S8), therefore the time series of vertical displacement of these stations are proportional to the caldera sill opening. If the GPS stations record deformation produced by a single source, then the source pressure function is the same for all the GPS stations. The only difference between the time series is the deformation amplitude which is a function of the source geometry and is a constant for each GPS station. Hence the time series can be normalized to account for this constant (Figure 7). The best-fit magma injection model for the normalized vertical component of the WLWY, LKWY and OFW2 stations predicts a transition time of 0.66 years and an exponential time constant of 4 years, with a final adimensional amplitude of 1.37. This implies that the magma injection model predicts ground uplift for at least 5 additional years should inelastic effects be absent, like fluid extraction outside of the caldera ((*Waite and Smith*, 2002)). Inversions for the best-fit magma injection model to the IS2 and GPS time series predict similar time constants and therefore similar properties of the plumbing system (Figure 7a), but a shorter transition due to the lack of InSAR data between September 2004 and May 2005. Therefore, the InSAR data are not considered further for these dynamic models. The magma injection model is also applied to GPS time series during 2014-2015, when fast uplift at NGB transitioned to subsidence following a Mw 4.9 earthquake on March 30 2014. The model results in good data fits (Figure 8), but the prediction of a single exponential decreasing trend is nearly identical to that of the double exponential model. In this latter model the pressure in the deep magma source is constant during the whole episode ((*Lengline et al.*, 2008)). The InSAR and GPS data and the magma injection model suggest that caldera uplift at Yellowstone during 2004-2009 and 2014-2015 is directly indicative of magma injection. Nevertheless, the magma composition cannot be estimated without inferences on the conduit radius (e.g., (*Pedersen and Sigmundsson*, 2006; *Fukushima et al.*, 2010; *Delgado et al.*, 2018)) and the source volume ((*Segall*, 2019)), the latter not available from the Okada model. The model indicates that magma injection into the caldera source explains the ground deformation with no need for pressurization due to volatile exsolution at the top of the plumbing system or at the bottom of the shallow hydrothermal system. This is in contradiction with an hybrid model of magma injection and volatile exsolution ((*Dzurisin et al.*, 2012)). The magma injection model also ignores the contemporary deflation at NGB, which we address in the following section.

5.1 Two pressurized reservoirs connected to a mantle magma source

The geodetic data show that uplift at the caldera floor is coeval to subsidence at the NGB during most of the 2004-2009 episode of unrest, and that two sub-horizontal sills are responsible for the deformation signals. In this section we use a simple fluid-solid mechanics model based on mass conservation to unravel the potential connection between these two sources of deformation. As our goal is to provide a simple physical model that allows to understand, not model the first order trends observed in the GPS time series, we make several geometrical and mechanical simplifications.

In this model, basaltic magma is injected to the shallow caldera source from both the mantle and a deep crustal sources beneath NGB (Figure 9). Although there is clear evidence for lateral transfer and storage of fluids between the SCD and MLD domes (Figure 5), these effects are of secondary order with respect to a single zone of magma accumulation along the two domes. The model of magma flow for two deformation sources embedded in an homogeneous linear elastic half-space is based on a mass balance the couples the reservoirs volume and pressure changes with the Poiseuille flow law. These equations are presented in previous studies (*Lengline et al.* (2008); *Segall* (2013); *Reverso et al.* (2014); *Le Mével et al.* (2016); *Walwer et al.* (2019)) and we adapt them for the specific case of Yellowstone. Since the pressure is proportional to the displacement in a linear elastic half-space, ground deformation follows the same temporal function than the source pressure function. More complex rheologies like viscoelasticity or other mechanisms of fluid transfer such as a flow in a poroelastic media ((*Hurwitz et al.*, 2007a)) are not considered in this study. Also, the model considers neither the mechanical interaction between the sources (e.g., (*Pascal et al.*, 2014)) nor the lateral offset between the sill centroids which are not symmetric and do not lie on top of each other. We assume that since the sources are very large, these boundary effect have a secondary effect. For simplicity we also neglect the short time lag between the onset of inflation at SC and ML and the deflation at NGB. We also neglect the complexity of Yellowstone's plumbing system inferred from seismic tomography ((*Farrell et al.*, 2014; *Huang et al.*, 2015)), including large areas of partial melt, multiphase components in the magma (crystals, dissolved and exsolved CO_2 and H_2O). More complex rheologies such as elastic layering, viscoelasticity and plastic effects are not considered. We do consider the effect of magma compressibility due to variations in the reservoir pressure (e.g., (*Rivalta*, 2010)).

The volume change rate in the two reservoirs connected with each other, and one of them fed by a mantle magma source is derived from mass conservation and is given by Equation 3 - Equation 4 (Figure 9, e.g., *Reverso et al.* (2014); *Walwer et al.* (2019))

$$\frac{d\Delta M_s}{dt} = \rho_m \frac{d\Delta V_s}{dt} = \rho_m (Q_{in} + Q) \tag{3}$$

$$\frac{d\Delta M_d}{dt} = \rho_{m_2} \frac{d\Delta V_d}{dt} = -\rho_{m2} Q_{in} \tag{4}$$

with $\Delta M_s, \Delta M_d$ the mass change in the shallow ($_s$) and deep reservoirs ($_d$), ρ_m, ρ_{m_2} the magma density that is injected in the shallow and deep reservoirs, $\Delta V_s, \Delta V_d$ the volume change in the shallow and deep reservoirs, Q the volume flux from a deep mantle source, and Q_{in} the volume flux from the NGB to the caldera source reservoir. Here the shallow and deep reservoirs represent the caldera source and the NGB sill-like sources. The relation between the volume change $\Delta V_{s,d}$ and the resulting reservoir overpressure $\Delta P_{s,d}$ under the assumption that magma is incompressible and the density is constant is Equation 5

$$\Delta V_{s,d} = \Delta P_{s,d} \frac{\pi a_{s,d}^3 \gamma}{G} \tag{5}$$

with γ equal to 1 for a sphere ((*McTigue*, 1987)) and $\frac{8(1-\nu)}{3\pi}$ for a penny-shaped crack ((*Fialko et al.*, 2001b)), G the shear modulus and $a_{s,d}^3$ the sphere/crack radius.

For the general case of volume change due to a pressure change in a reservoir (Equation 6)

$$\Delta P_{s,d} = \frac{\Delta V_{s,d}}{R_{s,d}(\beta_m + \beta_w)} \tag{6}$$

with R the reservoir volume, β_m the magma compressibility and β_w the reservoir compressibility. This results in the Equation 7

$$\Delta V_{s,d} = \Delta P_{s,d}(\frac{\pi a_{s,d}^3 \gamma}{G} + R_{s,d}\beta_m) \tag{7}$$

The volume flux in a vertical conduit connecting a mantle magma source $\Delta\bar{P}$ to a shallow source ΔP_s is given by the Poiseuille law in Equation 8

$$Q = \frac{\pi a^4}{8\mu H}(\Delta\rho g H + \Delta\bar{P} - \Delta P_s) \tag{8}$$

with a the conduit radius, μ the magma viscosity, H the conduit length, $\Delta\rho$ the magma-host rock density contrast, g the gravitational acceleration and $\bar{P}$ the mantle magma pressure ((*Jaupart and Tait*, 1990; *Lengline et al.*, 2008)). The expression is nearly identical for the conduit connecting the shallow and the deep source in Equation 9

$$Q_{in} = \frac{\pi a_2^4}{8\mu_2 H_2}(\Delta\rho_2 g H_2 + \Delta P_d - \Delta P_s) \tag{9}$$

with H_2, a_2 and μ_2 the conduit length, radius and magma viscosity in this conduit and ΔP_d the deeper reservoir. Here the flow from the deep reservoir depends upon the pressure gradient ((*Segall*, 2013)) instead of a constant magma flow ((*Reverso et al.*, 2014)). Combining Equation 3 - Equation 9 results in two equations for the pressure change of the two pressurized reservoirs (Equation 10 - Equation 11).

$$\frac{d\Delta P_s}{dt} = \frac{a_2^4 G}{8\mu_2 H_2 a_s^3 \gamma}(\Delta\rho_2 g H_2 + \Delta P_d - \Delta P_s) + \frac{a^4 G}{8\mu H a_s^3 \gamma}(\Delta\rho g H + \Delta\bar{P} - \Delta P_s) \tag{10}$$

$$\frac{d\Delta P_d}{dt} = -\frac{a_2^4 G}{8\mu_2 H_2 a_d^3 \gamma}(\Delta\rho_2 g H_2 + \Delta P_d - \Delta P_s) \tag{11}$$

We set

$$\begin{aligned} \tau_2^{-1} &= \beta = \frac{a_2^4 G}{8\mu_2 H_2 a_s^3 \gamma} \\ \tau_1^{-1} &= \alpha = \frac{a^4 G}{8\mu H a_s^3 \gamma} \\ \tau_3^{-1} &= \epsilon = \frac{a_2^4 G}{8\mu_2 H_2 a_d^3 \gamma} \end{aligned} \tag{12}$$

If magma compressibility is taken into account, then the time constants become

$$\begin{aligned} \beta &= \frac{\pi a_2^4 G}{8\mu_2 H_2(\pi a_s^3 \gamma + G R_s \beta_m)} \\ \alpha &= \frac{\pi a^4 G}{8\mu H(\pi a_s^3 \gamma + G R_s \beta_m)} \\ \epsilon &= \frac{\pi a_2^4 G}{8\mu_2 H_2(\pi a_d^3 \gamma + G R_d \beta_m)} \end{aligned} \tag{13}$$

Arranging terms results in Equation 14 - Equation 15

$$\frac{d\Delta P_s}{dt} = -P_s(\alpha + \beta) + P_d\beta + \alpha(\Delta\bar{P} + \Delta\rho g H + \Delta\rho_2 g H_2) \tag{14}$$

$$\frac{d\Delta P_d}{dt} = P_s\epsilon - P_d\epsilon - \epsilon\Delta\rho_2 g H_2 \tag{15}$$

Equation 14 - Equation 15 form a linear system of non-homogeneous differential equations that can be casted in matrix form (Equation 16 - Equation 17)

$$\begin{bmatrix} \frac{d\Delta P_s}{dt} \\ \frac{d\Delta P_d}{dt} \end{bmatrix} = \begin{bmatrix} -\alpha-\beta & \beta \\ \epsilon & -\epsilon \end{bmatrix} \begin{bmatrix} \Delta P_s \\ \Delta P_d \end{bmatrix} + \begin{bmatrix} \beta\Delta\rho_2 g H_2 + \alpha\Delta\rho g H + \alpha\Delta\bar{P} \\ -\epsilon\Delta\rho_2 g H_2 \end{bmatrix} \tag{16}$$

$$\frac{d\bar{P}}{dt} = G\bar{P} + H \tag{17}$$

with $\bar{P} = [\Delta P_s, \Delta P_d]^T$ the vector that contains the functions for the shallow and deep reservoir pressure. Instead of a piecewise mantle source pressure function of a linear increase followed by a constant after a time threshold ((*Le Mével et al.*, 2016)), we use an exponential function of the form $\Delta\bar{P} = \bar{P}(1 - e^{-\frac{t}{\tau_m}})$ because it is easier to integrate. This function is derived from the data itself (Figure 7) with $\tau_m = 0.36$ years. The solution to Equation 17 is a function of the form $\vec{P(t)} = \vec{v_1}e^{\lambda_1 t} + \vec{v_2}e^{\lambda_2 t} + \vec{a}e^{-\frac{t}{\tau_m}} + \vec{b}$ with $\vec{v_{1,2}}$ and $\lambda_{1,2}$ the eigenvectors and eigenvalues of G and the last two terms are vectors derived from the method of undetermined coefficients for the non-homogeneous terms (last term on the right-hand side of Equation 17). The final solution for initial conditions $P_s(0) = 0$,$P_d(0) = P_{d_0}$ is Equation 18

$$\begin{bmatrix} \Delta P_s \\ \Delta P_d \end{bmatrix} = C_1 e^{\lambda_1 t} \begin{bmatrix} 1 + \frac{\lambda_1}{\epsilon} \\ 1 \end{bmatrix} + C_2 e^{\lambda_2 t} \begin{bmatrix} 1 + \frac{\lambda_2}{\epsilon} \\ 1 \end{bmatrix} + \begin{bmatrix} a_1 \\ a_2 \end{bmatrix} e^{-\frac{t}{\tau_m}} + \begin{bmatrix} b_1 \\ b_2 \end{bmatrix} \tag{18}$$

with the eigenvalues $\lambda_{1,2}$

$$\lambda_{1,2} = \frac{-(\alpha + \beta + \epsilon) \pm \sqrt{(\alpha^2 + \beta^2 + \epsilon^2 + 2\alpha\beta + 2\beta\epsilon - 2\alpha\epsilon)}}{2} \tag{19}$$

and constants

$$\begin{aligned} b_1 &= \bar{P} + \Delta\rho g H \\ b_2 &= \bar{P} + \Delta\rho g H - \Delta\rho_2 g H_2 \\ C_1 &= P_{d_0} - (C_2 + a_2 + b_2) \\ C_2 &= \epsilon\frac{(P_{d_0} - a_2 - b_2)(1 + \lambda_1/\epsilon) + a_1 + b_1}{\lambda_1 - \lambda_2} \end{aligned} \tag{20}$$

Here P_{d_0} is the overpressure produced by injection of basaltic magma at the NGB reservoir during 1996-2000 ((*Wicks et al.*, 2006)). Since basaltic magma is unlikely to significantly cool to produce a significant density change in 4 years, for simplicity we assume that $\Delta\rho = \Delta\rho_2$, $\mu = \mu_2$.

The selected model parameters are in Table 3. Since there are no geophysical constrains on the fourth power of the conduit radius R^4 and the viscosity of the injecting basalt μ, we parametrize the model in terms of the conduit conductivity $\bar{c} = R^4/\mu$ ((*Anderson and Segall*, 2013)). Basaltic melts have viscosities of $10 - 10^2$ Pa s ((*Giordano and Dingwell*, 2003)) and conduit flow models during episodes of unrest in basaltic volcanoes show radii of ∼1 m ((*Pedersen and Sigmundsson*, 2006; *Fukushima et al.*, 2010)), resulting in $\bar{c} \sim 0.1 - 0.01\frac{m^4}{Pas}$. The initial pressure with respect to lithostatic conditions are $P_s^0 = 0$ MPa and $P_d^0 = 0 - 0.5$ MPa, the latter value arising due to the potential magma injection at NGB during 1996-2000 ((*Wicks et al.*, 2006)). The amplitude of the source pressure just scales the pressurization of the reservoirs, so it is not relevant since we are interested on the temporal evolution of the reservoir pressures. We consider cases with and without a density difference, in which the magma ascends due to its overpressure and due to the combined overpressure and buoyancy effects.

The simulations show that magma ascends due to its overpressure only (Figure 10a-b), predicting the same double exponential pattern for both the caldera source and the NGB source, albeit with a lower amplitude for the latter. However, the model for $P_d^0 = 0$ MPa is unable to predict a double exponential pressurization for the caldera source and a linear depressurization for the NGB source. This is a rather unrealistic scenario as the model predicts that magma ascends from the mantle to the shallow reservoir, and then the high magma overpressure implies that the NGB reservoir must inflate in response to the overpressure, with magma descending 2 km. The effect of magma compressibility is of second order due to the large dimensions of Yellowstone's plumbing system and does not change significantly the sources pressure changes. However, increasing the magma compressibility significantly increases the volume of intruded magma in the reservoir (e.g., Figure 9 in (*Le Mével et al.*, 2016)).

On the other hand the simulations show that when magma ascends due to buoyancy and overpressure (Figure 10c-d), the models predicts pressurization with an exponential increase and decrease at the caldera source and both depressurization and pressurization at NGB with near linear trends (Figure 7c-d). We note that the magnitude of the pressurization of the buoyancy and overpressure model is one of order magnitude larger than the model with magma overpressure only. The only possibility to significantly depressurize the NGB source due to magma flow to the caldera source is to set $P_d^0 = 0 = 0.5$ MPa (Figure 11) and with $\bar{c} \sim 10^0\frac{m^4}{Pas}$ or smaller but as this value is increased, the magnitude of the subsidence decreases in response to a better hydraulic connection. This is a plausible scenario since it is likely that previous episodes of uplift are inferred to have occurred at NGB ((*Wicks et al.*, 2020)). The simulation predicts subsidence at NGB and double exponential uplift at the caldera, but eventually all the subsidence from material extracted from NGB is counterbalanced by the fluid influx from the caldera source to NGB. The MBEM model predicts ΔP=∼0.08 MPa for the caldera source, but it is very unlikely that the NGB reservoir overpressure reached such value during 1996-2000 because the amplitude of uplift during that time span is much lower than the caldera uplift during 2004-2009. This implies than in this scenario the NGB reservoir should have been pressurized decades before 1996, for which we have no quantitative constrains.

An alternative model considers that the deep source of magma injection is located below NGB and not below the caldera. Therefore basalt ascends to NGB and then to the caldera, potentially resulting in depressurization during several years at NGB. In this case the second term in the right hand side of Equation 10 must be included in the right hand side of Equation 11 after switching ΔP_s with ΔP_d and modifying the time constant for the NGB reservoir. We also assume a slight overpressure for the NGB source. Changing the force balance with the same pressure function for the mantle source does not result in depressurization for the NGB source for more than 1.5 years until it will start to inflate in response to the incoming magma from the mantle (not shown).

Regardless of the model, none of these simulations can predict at the same time the trends observed in the InSAR and GPS time series at both the caldera floor and NGB and with a constrained set of assumptions available since geodetic measurements started in 1975.

6 Discussion

6.1 Source models and comparison with previous studies

Two families of source models have been proposed for the 2004-2009 episode of unrest: those that rely on horizontal dislocations ((*Chang et al.*, 2007,0; *Wicks et al.*, 2020), this study) and those that use a combination of pressure sources ((*Aly and Cochran*, 2011; *Tizzani et al.*, 2015)). Although both type of models can fit the data well, we consider that the dislocations are more realistic. First, they require less model parameters. Second, neglecting the mechanical interaction between two sills is less inaccurate than neglecting the interaction between at least three pressure sources ((*Aly and Cochran*, 2011; *Tizzani et al.*, 2015)). Our results are similar to those of (*Chang et al.*, 2007,0) who also found two rectangular dislocations at depths of ~7-10 and ~7-13 km for the caldera and NGB sources, albeit modeling very small data sets. The caldera source model is located at the top of the low V_P zone below the caldera imaged with three-dimensional P wave tomography. This zone has -3 to -4% of V_P difference with respect to the reference velocity model and is inferred to contain little to none partial melt resolvable by this geophysical method ((*Farrell et al.*, 2014; *Huang et al.*, 2015)). Since the magma injection is a discrete event with respect to the spatially and time averaged resolution of seismic tomography, we see no contradiction between the geodetic sources and lack of a clear V_P anomaly. (*Wicks et al.*, 1998, 2006) have argued for two discrete sources of deformation below the caldera floor and episodically active over different times but both the uniform and distributed (Figure 4, Figure S5) opening models indicate that a single dislocation can explain most of the deformation signal during 2004-2009. The caldera source has no clear boundary between the magma accumulation zones below SCD and MLD, except for localized uplift at the SCD, resulting in an additional 5 cm of uplift with respect to MLD. Given the few cycles of deformation observed with detailed geodetic observations, it is not possible to assess if the discrete storage zones below the MLD and SCD ((*Wicks et al.*, 2006, 1998)) are representative of caldera uplift during longer periods of time or not. The NGB source is significantly shallower and different with respect to the source that uplifted during 1996-2000 located at a depth of 16 km ((*Wicks et al.*, 2020)), vs 10.7 during 2004-2009. Another difference with respect to (*Chang et al.*, 2007,0) models is that a significant part of the NGB source is located below the caldera floor, and not adjacent to it.

Changes in the source geometry can be assessed comparing the location and wavelength of the deformation signals for the different episodes of uplift for data sets that were acquired with the same or very similar flight direction, radar beam and look angle. These data sets include ERS-1/2 descending interferograms and a stack (Figure S4), the ENVISAT IM2 data (Figure 2) and the TSX descending stack. Here the ERS-1/2 and ENVISAT IM2 are from the the same track so they have the same line-of-sight. This analysis shows that the wavelength and location of the deformation signals varies during the periods of caldera subsidence in 1992-1995 ((*Wicks et al.*, 1998; *Aly and Cochran*, 2011), Figure S4), uplift 1996-1997 (Figure 2F in (*Wicks et al.*, 1998)), subsidence 2000-2002 (Figures 2b-c in (*Wicks et al.*, 2006)), uplift 2004-2009 (Figure 2), subsidence 2010-2013 (Figure 2), uplift 2014-2015 ((*Wicks et al.*, 2020), Figure 8) and subsidence 2015-2020 (Figure 1 in (*Wicks et al.*, 2020)). Deformation at NGB also shows differences in location and wavelength of the deformation signal during the episodes of uplift in 1996-2000 ((*Wicks et al.*, 2006), Figure S4), subsidence during 2004-2008 (Figure 2), uplift during early 2014, subsidence during the rest of 2014 (Fig 2B in (*Wicks et al.*, 2020)) and uplift during 2015-2019 (Fig 1 in (*Wicks et al.*, 2020)). This implies that the deformation sources are not stable over and they slightly change from one cycle of either uplift or subsidence to the next one. In contrast, other volcanoes show stable deformation sources over several cycles of deformation, even after eruptions ((*Lu et al.*, 2010; *Lu and Dzurisin*, 2010; *Delgado*, 2020)). The lack of stationary sources indicates patterns of migrating fluids towards shallower depths ((*Wicks et al.*, 2020)) and hampers the use of magma dynamics models that rely on a single stable source in depth and location to explain long cycles of unrest (e.g., (*Giudicepietro et al.*, 2017)). The spatial variability also indicates a highly dynamic plumbing system, akin to a crystal mush where unrest occurs episodically and in discrete zones of the mush ((*Cashman et al.*, 2017)). On the other hand, do the deformation data indicate a trans-crustal magmatic system in which unrest occurs at multiple depth levels in the crust? The variability in the source depths suggests that this actually occurs at Yellowstone, even on short time scales of less than one year, like during the NGB uplift in early 2014 (Figure 1). However, the exact pattern of fluid migration, potential magma mixing and mingling and stress interaction (e.g., (*Albino and Sigmundsson*, 2014)) are yet to be unravelled.

6.2 Driving mechanisms of unrest

On a geological time scale, the driving mechanism of unrest at Yellowstone caldera are discrete pulses of basalt injection at the base of the rhyolitic plumbing system below the caldera and NGB. (*Lowenstern and Hurwitz*, 2008) calculated that $\sim$0.3 km^3/yr of basalt intrusion with 1 wt% of dissolved CO_2 are required to account for the measured flux of passive CO_2 degassing at Yellowstone, 4 times larger than the time-averaged rate of $\sim$0.074 km^3/yr during 2004-2009. A direct comparison between these data sets is not possible due to the episodic nature of magma injection and the lack of continuous time-lapse measurements of CO_2 degassing, discussed in detail later. The mechanisms of unrest are less clear over shorter time scales due to the coupling of the shallow hydrothermal system with the deeper magmatic system and volatile exsolution from the injecting basalt ((*Dzurisin et al.*, 2012)). Also, independent data sets and models suggest contradicting mechanisms. Yellowstone lake shorelines have tilted terraces such that the caldera subsidence slightly exceeds caldera uplift during the Holocene ((*Pierce et al.*, 2002)). To account for the slight subsidence, the volume change of exsolved volatiles extracted from the caldera must exceed the volume of injected magma, and these events must alternate in time. This lead (*Pierce et al.*, 2002) to suggest that the buildup and extraction of magmatic volatiles is a more likely explanation for the slightly higher subsidence in the Holocene than magma injection. Further, (*Fournier*, 1989) showed that a crystallizing magma can release 0.026 km^3/yr of exsolved fluids from that trapped below the self-sealed layer. This is enough to account for the volume changes that produced the caldera uplift during 1923-1975. However, the hydrothermal model cannot explain the transition from uplift to subsidence because the seismic swarms that have been recorded coevally to the transition require magma injection. The swarms are likely due to the episodic breaching of a self-sealed at the BDT that leads to fluid extraction from the caldera ((*Waite and Smith*, 2002)). This process is highly enhanced by a deepening of the BDT, produced by an increase in the strain rate due to episodic magma injection ((*Fournier*, 2007)), contradicting the previous mechanisms for unrest due to volatile pressurization and extraction.

Thereby, (*Dzurisin et al.*, 2012) favor a conceptual model that reconciles a wide range of geological, geochemical and geophysical observations. This model suggests that episodic batches of basalt are injected at the base of the rhyolitic crystal mush resulting in reservoir pressurization either at NGB or SCD. As the basalt and the mush crystallize, magmatic volatiles are exsolved. These fluids are in a supercritical state that are trapped below a self-sealed layer in the lower parts of the hydrothermal system and the upper section of the magmatic system resulting in reservoir pressurization and caldera uplift. The self-sealed layer is also the BDT. Magma injection increases the strain rate, which temporarily deepens the BDT. In this scenario, fluids in the plastic zone at near lithostatic pressures eventually breach the self-sealed layer, leading to seismic swarms in distal parts of the caldera ((*Waite and Smith*, 2002)), fluid migration outside of the caldera and ground subsidence ((*Fournier*, 1989, 2007)). On the other hand, long-term subsidence at the caldera is likely produced by volatile exsolution from the crystallizing rhyolitic mush that also migrates outside of the caldera ((*Dzurisin et al.*, 1990)). However, (*Dzurisin et al.*, 2012) model does not allow to assess the relative contributions of magma injection and volatile exsolution in the reservoir pressurization (e.g., (*Tait et al.*, 1989)) and the fluids sink sources. Therefore, we compare our results with the previous studies.

The LKWY, WLWY and OFW2 GPS fit to the magma injection model (Figure 7) is a strong indication that the driving mechanism of uplift for the caldera source is the injection of $\sim$0.35 km^3 of incompressible basalt during 2004-2009, with no need to argue for exsolved volatiles (discussed later). In this model the pressure of the deep magma source increased linearly until it reached a threshold in early 2005, then it remained constant. This results in a time-variable uplift rate that increased exponentially and then decreased exponentially after 2005 until the hydraulic connection with the deep mantle source was shutdown by inelastic processes (discussed later). Magma is injected in the upper part of the mushy plumbing system inferred from seismic tomography ((*Farrell et al.*, 2014; *Huang et al.*, 2015)). This is also valid for the caldera uplift during 2014-2015 – magma injection at the caldera with source pressure functions that vary from one episode to the next one and a connection between the caldera and NGB sources. On the other hand, there are significant differences. First, the NGB reservoir during 2014-2015 is significantly shallower at a depth of 1-4.5 km ((*Wicks et al.*, 2020; *Dzurisin et al.*, 2019)) vs 10.7 km for 2004-2009, leading (*Wicks et al.*, 2020) to suggest a source of hydrothermal origin. Therefore, we discard that the subsidence at NGB during 2014 would result from magma transfer from this source into the much deeper caldera source, located at a depth of $\sim$6 km during 2014 ((*Wicks et al.*, 2020)). Hence, the model of two connected reservoirs cannot be applied to this episode of uplift. We speculate that the reversal from uplift to subsidence at NGB in March 2014 resulted from fluid migration into the shallow hydrothermal system following the breaching of the self-sealed layer that separates the BDT. Since the caldera source did not change its behaviour when NGB uplifted in early 2014 (Figure 8), we speculate that the BDT breaching might have changed the stress field in the deeper source (e.g., (*Albino and Sigmundsson*, 2014)), potentially allowing for magma to be injected from a mantle source. The exact mechanism is beyond the scope of this study.

One significant caveat of the magma injection models is that they do not consider at all the complex structure of Yellowstone's underlying plumbing system inferred from local and teleseismic tomographies ((*Farrell et al.*, 2014; *Huang et al.*, 2015)). These studies show that the volcano is underlain by a low V_p anomaly at depths of 5-17 km with 5-15% of melt fraction interpreted as a rhyolitic partial melt underlain by basaltic partial melt. Another low velocity zone is located at depths of 20 to 50 km, with a melt fraction of 2%, extending to the Moho and also interpreted as basaltic partial melt. The two low velocity zones are physically separated. The previous magma injection models neither consider how magma bypasses or interacts in some way with these very large areas of partial melt nor how can the melt segregate through the porous crystalline matrix to ascend through the crystal mush that likely exists in the upper crust. Further, the magma injected during 2004-2009 likely has a basaltic chemical composition compared to that of the mushy rhyolitic reservoir, and they might eventually coalesce on time scales of 10^4 - 10^4 years (e.g., (*Biggs and Annen*, 2019)). Magma can also stall somewhere in the crust in a level of neutral buoyancy and undergo viscosity changes resulting from phase transitions. This process could occur deep in the crust such that it might not be detectable with the data. However, the data does not show that the deformation sources change during the episode of uplift. It is unclear from a modeling point of view how the ascending basalt interacts with the plumbing system in the framework of a transcrustal model of unrest on multiple levels in the crust ((*Cashman et al.*, 2017; *Sparks et al.*, 2019; *Sparks and Cashman*, 2017)). These are all points that have to be addressed in future studies that relax the restrictive assumptions made in the models of magma injection (Figure 9).

The spatial coincidence of the SCD with the area of maximum uplift has led other studies to suggest that this is the main area of magma injection ((*Wicks et al.*, 2006; *Chang et al.*, 2007)). Despite the uplift started simultaneously for SCD and MLD in July 2004, we see no clear evidence in the OFW2, WLWY and LKWY stations (Figure 1, Figure S1) to state that magma was first intruded at SCD and then it migrated to MLD, or that magma was injected at MLD and then was stored at SCD. Whatever the situation, this suggests a highly connected area of magma storage that responded coevally to the onset of magma injection with no clear boundary as shown by the distributed sill opening models (Figure 5). GPS observations in the middle of the caldera floor might help to address this point during future episodes of unrest.

Magma ascent resulting in reservoir pressurization is due to both its overpressure and its buoyancy with respect to the host rock (Equation 8-Equation 9). The model of connected reservoirs provide insights in this aspect (Figure 10). First, the model with both magma buoyancy and magma overpressure is unable to reproduce the double exponential signals observed at the caldera floor and the NGB, indicating that the signal observed in the GPS time series is indicative of magma overpressure only. This is not a unique characteristic of Yellowstone and has observed at other volcanoes (e.g., (*Le Mével et al.*, 2016)). Second, if buoyancy effects are neglected, then the NGB source inflates in response to the magma flux, resulting in a pressure function very similar to that of the caldera source. None of the aforementioned two models predict that subsidence at NGB should end with the waning of uplift at the caldera floor. Whatever the case, the model suggests that magma ascends solely due to its overpressure, and that the subsidence at NGB cannot be explained due to magma extraction towards the caldera source. If NGB is connected to the caldera source, it is not by a mechanism of Newtonian conduit flow.

Any mechanism that explains the subsidence at NGB must take into account the very similar onset of uplift with respect to the caldera source, implying that the subsidence is to same extent triggered by magma injection at the caldera. The hydrothermal system is shallower than 5 km ((*Fournier*, 1989)), so the 2004-2009 NGB source is too deep to be considered of hydrothermal origin. (*Chang et al.*, 2007) explained the relation between NGB and the caldera by a mechanism in which the caldera sill opening produces positive dilatation up to $3\times10^{-}5$ strain next to the crack tip. This value is one order of magnitude above the smallest measured strain change produced by dynamic earthquake triggering that can induce transient increases in the medium permeability ((*Manga et al.*, 2012)). This mechanism can induce flow of magmatic volatiles from NGB to the caldera and trigger microseismicity between these two sources. Although the mechanism is plausible, there is a caveat. The NGB sill is located below the BDT and the surrounding medium is plastic with little to none permeability that fluids can use to migrate between the sources. Therefore an opening sill should not produce an increase in the medium permeability because there is no primary porosity ((*Fournier*, 2007)). The permeability can be increased by magma injection which increases the strain rate, deepening the BDT by ∼1 km, resulting in a change in the rheological properties and brings deep zones that are plastic into a brittle behavior for a short period of time. However, the NGB and caldera sills are too deep to lie in the brittle region even after the transient increase in the strain rate. Further, lowering the BDT usually results in the breaching of the layer that separates the BDT, not in fractures in zones that are deep into the plastic zone. This implies that the permeability mechanism of magma transport is also not feasible and the connection between NGB and the caldera is uncertain.

We have shown that the geodetic signals during the episode of caldera uplift can be explained entirely by magma injection, with no need to invoke volatile exsolution. But this model is neither unique nor necessarily the best explanation. It does not imply that during other episodes of ground uplift magma injection or other mechanisms on unrest can also produce the exact same geodetic signal. For example, rhyolitic plumbing systems are crystal mushes (e.g., (*Bachmann and Bergantz*, 2008)) and Yellowstone's plumbing system has limited amounts of melt ((*Farrell et al.*, 2014; *Huang et al.*, 2015)). Here, exsolved fluids can percolate through the porous matrix and ascend to the top of mush where they accumulate in sill-like discrete areas. As the volume of fluids increase this can also result in sill pressurization and ground deformation (e.g., (*Sparks et al.*, 2019)). On the other hand, is it possible that the fluid exsolution, permeable flow and fluid accumulation at the liquid-rich mush cap does not result in detectable pressurization during the caldera uplift? Is it possible that any significant fluid exsolution occurs only in response to the depressurization of the self-sealed layer after it is breached? This seems unlikely. For example, fluid exsolution is not enhanced if the minimum principal stress equals the lithostatic load until the latter equals the pore-fluid pressure (section 10.4.2 in (*Fournier*, 2007)), and this could be attained only after a certain amount of magma has been injected. Further, the mechanisms can vary significantly from an episode to the next one (*Fournier* (2007)), and mechanisms of unrest that last 10^0 - 10^1 years might not be representative of the overall caldera behaviour during time scales of 10^4 - 10^5 years (e.g., (*Pierce et al.*, 2002)). These scenarios were not considered in this study but are geologically plausible, so future studies should address them.

6.3 Comparison with seismicity, microgravity and stream/gas geochemistry

Ground deformation is one of the several indicators of volcano unrest but uncertainties in the mechanisms that result in ground uplift imply that these data should be analyzed and compared jointly with other independent data sets ((*Pritchard et al.*, 2019)). Here we compare the deformation during the episode of uplift with the dense seismic (e.g., (*Waite and Smith*, 2002; *Farrell et al.*, 2014)) and geochemical ((*Lowenstern et al.*, 2017)) data acquired during more than 30 years at Yellowstone.

Statistics of the number of earthquakes per quarter do not show any abnormal trends during 2004-2008 (Figure 1B in (*Chang et al.*, 2007,0), Figure 8 in (*Shelly et al.*, 2013), Figure 1 in (*Farrell et al.*, 2014)). The largest clusters of earthquakes in the caldera during the episode of uplift (Figure 1) occurred during 2004-2006 with microseismicity located at the northern edge of the caldera floor ((*Chang et al.*, 2007), not shown in Figure 1), and during the December 2008 swarm at Yellowstone Lake ((*Farrell et al.*, 2010)). The seismicity with $M_L > 2.5$ at the onset of uplift is scattered across the caldera with no clear clusters and significantly less than the seismicity triggered when the uplift transitions to subsidence ((*Shelly et al.*, 2013)). Focal mechanisms calculated from waveform first arrivals show normal faulting with seismicity clusters towards the N and S parts of the caldera and with only four events at the SCD ((*Russo et al.*, 2017)). (*Taira et al.*, 2010) analyzed five M3+ earthquakes during 2007-2009, two of them the first non-double couple focal mechanisms since monitoring started in 1975. These earthquakes are triggered by fluid migration due to an increase in dilatation from the sill towards shallower opening cracks. (*Farrell et al.*, 2009) calculated the b-value from the Gutenberg-Richter law in a de-swarmed earthquake catalog from 1973 to 2006, showing high b-values next to MLD, but no abnormal values indicative of fluid injection at the SCD. In general we conclude that the 2004-2009 caldera uplift was not related to abnormal seismicity in response to magma injection compared with the seismic swarms when deformation shifts from uplift to subsidence ((*Waite and Smith*, 2002; *Shelly et al.*, 2013)). This is in contrast with other volcampes, like Long Valley caldera where the onset ground uplift is correlated with increases in seismicity (Fig 3a in (*Hill et al.*, 2020)). The lack of abnormal seismicity during 2004 is not unique of Yellowstone as other volcanoes with very fast deformation, either basaltic like Sierra Negra ((*Davidge et al.*, 2017)), or rhyolitic like Cordón Caulle ((*Delgado et al.*, 2018)) are accompanied by limited amounts of seismicity. One potential explanation for the overall lack of abnormal seismicity is that the plastic rocks around the rhyolitic reservoir cannot be fractured except at the end of the cycles of uplift when the rocks behave in a brittle way for short periods of time. Another alternative is that the 2004-2009 cycle of uplift did not produce significant seismicity due to the Kaiser effect ((*Heimisson et al.*, 2015)). Here fracturing and seismicity are produced only if the medium is stressed above a previous threshold than in a loading cycle already resulted in fracturing. However, this hypothesis can not be proved as either true or false because only two cycles of uplift in 1923-1984 and 1996-1997 before 2004 were recorded with instrumental observations, both with a significantly worst temporal sampling than the 2004-2009 cycle.

Micro-gravity data were only measured during 2007-2012 ((*Farrell*, 2014)), and then since 2017 ((*Poland and Zeeuwvan Dalfsen*, 2019)). The 2007-2012 data did not show clear gravity changes but as the data did not include high quality elevation measurements for each gravity station, it did not provide insights on any particular geological process ((*Poland and Zeeuwvan Dalfsen*, 2019)). Therefore the gravity data cannot be directly compared with the InSAR and GPS observations during 2004-2009. (*Poland and Zeeuwvan Dalfsen*, 2019) measured gravity variations four times during 2017 and concluded that the gravity uncertainty of $\sim$20 mGal on stable benchmarks is low enough to detect mass changes due to magma injection.

In terms of gas and fluid geochemistry, despite the many decades of sampling at Yellowstone's hydrothermal fields (e.g., (*Lowenstern et al.*, 2017)), there is a dearth of long-term geochemical time series. Continuous measurements of CO_2 with eddy covariance instruments have been underway only since 2016 ((*Lewicki et al.*, 2017)). High temporal resolution water chemistry measurements at the Upper Geyser Basin during 2007-2008 ((*Hurwitz et al.*, 2012)) and in major rivers during 2001-2004 and 2006-2007 ((*Hurwitz et al.*, 2007b,0)) cannot be compared with the episode of caldera uplift due to their low temporal sampling, or being too distant from the areas of unrest. Decadal time-lapse measurements are only available for chloride discharges in streams with a yearly temporal sampling, but these measurements did not show any unambiguous trend that deviates from the base level values during the period of caldera uplift ((*Hurwitz and Lowenstern*, 2014)). Furthermore, a lateral redistribution of the abnormal chloride flux due to basalt injection would take years to decades until it would result in abnormal fluxes in streams and therefore correlations with ground deformation are not expected to be detected ((*Hurwitz et al.*, 2007b)). These authors also concluded that it would be more feasible to detect perturbations in the shallow hydrothermal system due to deep magma injection by tracking changes in the gas and steam flux instead of the river solute fluxes. Finally, correlations of older episodes of unrest with geochemistry of springs in the NW part of the caldera do not provide meaningful insights ((*Evans et al.*, 2006)).

We conclude that the 2004-2009 episode of caldera uplift was not correlated with other large-scale signs of unrest except during the December 2008 dike intrusion ((*Farrell et al.*, 2010)) and the transition from uplift to subsidence in January 2010 ((*Shelly et al.*, 2013)).

6.4 Eruptive potential of Yellowstone

Eruptions occur when the deviatoric stress in a pressurized reservoir reaches the tensile strength of the rock of ∼10-40 MPa producing a mode I crack that propagates to the Earth surface ((*Tait et al.*, 1989; *Pinel and Jaupart*, 2003; *Albino et al.*, 2010)). We use the source pressure change as a proxy for the tensile strength of the encasing rock at Yellowstone's magma reservoir. The MBEM inversion and penny-shaped crack approximation predict source overpressures of ∼0.08-0.13 MPa respectively (Figure S7). These values are several orders below the tensile strength of the rock of ∼10 MPa. Therefore individual pulses of uplift like those in 2004-2009 are very unlikely to lead to an eruption. Eruptions should occur every ∼100 cycles of uplift similar to that of 2004-2009. The recurrence interval of large-scale caldera uplift is not well constrained since geodetic observations with yearly temporal resolution started in 1975. If pressurization cycles last on the order of ∼5 years, the eruption recurrence is at least 500 years, although there is considerable uncertainty because the caldera uplift is highly transient, with variable magnitudes of magma injection and duration as well as the length of the quiescence periods. If we assume that for every episode of uplift there is an episode of quiescence or caldera subsidence of similar duration, then the eruptive frequency increases to 1 Kyrs. The last eruptions at Yellowstone occurred ∼70 Kyrs ago ((*Christiansen*, 2001)), which is more than one order of magnitude longer than our eruption interval. If the net record of deformation in the Holocene is slight subsidence, it implies that reservoir deflation is slightly larger than reservoir pressurization and hence the pulses of uplift are even less likely to result in an eruption ((*Pierce et al.*, 2002)).

Despite the small amount of pressurization, much lower than pressure changes in smaller sills elsewhere (e.g., (*Le Mével et al.*, 2016; *Delgado et al.*, 2016)), a seismic swarm interpreted as a small dike intrusion occurred in December 2008 - January 2009 ((*Farrell et al.*, 2010)). The material that intruded the dike was either rhyolitic magma or magma-derived aqueous fluids. The dike is offset with respect to the locus of maximum magma injection at the SCD. This dike produced small displacements recorded by the LKWY station (< than 1 cm, (*Farrell et al.*, 2010)), but the distributed opening model show residuals in the eastern part of Yellowstone Lake that could be explained by this small dike (Figure 4). One explanation is that this intrusion was triggered by reaching the tensile strength of the rock after thousands of loading cycles. Another alternative is that successive cycles of uplift and subsidence at the caldera floor might have decreased and permanently fractured the surrounding rock due to damage loading, effectively lowering the wall rock shear modulus and decreasing the rupture threshold ((*Carrier et al.*, 2015)). If this is true, cyclic pressurization that are unable to trigger a dike intrusion under the aforementioned standard rupture models ((*Pinel and Jaupart*, 2003; *Tait et al.*, 1989; *Albino et al.*, 2010)) can result in small dike intrusions that would not be observed otherwise. Another alternative is these rupture criteria are not valid for the geologic conditions of Yellowstone due to the very large plumbing system of this volcano and its weak crust. Another alternative is that it was not a dike intrusion but only a small swarm (*Shaul Hurwitz*, personal communication). Finally, another alternative is that the swarm was produced by leakage of a small amount of magmatic fluids above the BDT, but with no resulting subsidence until the next leakage one year later. Whatever the case, the eruptive potential of Yellowstone deserves a more thorough analysis relating the cyclic loading model with a detailed analysis of the seismic data (e.g., (*Carrier et al.*, 2015)).

6.5 Transition of uplift to subsidence

One of the most intriguing features of Yellowstone is the cyclic transition of uplift to subsidence with periods of ∼10 years (Figure 1). This transition has been explained by the breaching of a self-sealed layer at the BDT due to transient pressurization by either magma injection or exsolved fluids which migrate outside the caldera upon the layer breaching ((*Waite and Smith*, 2002; *Dzurisin et al.*, 2012)). The fluid migration occurs at the end of an uplift cycle and is coeval with seismic swarms in the distal parts of the caldera ((*Waite and Smith*, 2002; *Shelly et al.*, 2013)). Afterwards, the caldera subsides in response to migration of exsolved fluids from a crystallising mush for several years until another cycle resumes ((*Dzurisin et al.*, 1990)). Volumetric changes due to a cooling intrusion produce negligible volume changes and are unable to explain the caldera subsidence ((*Dzurisin et al.*, 1990)). In this model of cyclic deformation, the secular trend of subsidence due to volatile exsolution is reversed by highly transient pulses of basalt injection at the caldera, as in 2004-2009. The Madison Plateau swarm in January 2010 ((*Shelly et al.*, 2013), Figure 1) is interpreted as the breaching of self-sealed layer in the NW part of the caldera, and occurred during the transition from uplift to subsidence. In general, non-eruptive subsidence at volcanoes and calderas like Cerro Blanco ((*Pritchard and Simons*, 2004)), Askja ((*de Zeeuw-van Dalfsen et al.*, 2013)) and Medicine Lake ((*Poland et al.*, 2006)) show linear rates ∼2-3 cm/yr over time spans of decades. These have been related to cooling intrusions and a combination of other mechanisms like tectonic extension, but in the absence of a clear sink area, the exact mechanism of subsidence is quite uncertain.

The InSAR and GPS observations raise more questions than answers on the mechanisms of caldera subsidence. First, what is the sink of the magmatic fluids extracted from the NGB? (*Wicks et al.*, 2020) suggested that fluids extracted from NGB are injected either in the Norris-Mammoth corridor or the Hebgen Lake fault zone which are the zones with the highest amount of seismicity at Yellowstone. None of the post 2010 data show clear deformation signals outside of the caldera that could be sink sources for some fluids extracted from NGB and the caldera, although the small swath of the TSX data also introduces some uncertainty in this regard (Figure 2). It is also possible that the escaping fluids do not leave a clear geodetic signal if there is no sink reservoir to store them. This is in contrast with the post 2014 deformation which shows small-scale deformation that could reflect fluid pathways outside of the caldera (Fig 7 in (*Wicks et al.*, 2020)). Second, if the end of the caldera uplift is due to some inelastic mechanism of fluid migration above the BDT, then it implies that breaching the self-sealed layer changed the force balance on the conduit that feeds the caldera reservoir. Fluid migration outside of the caldera source implies that the pressure gradient driving this flow is much higher than the pressure gradient between the caldera and the mantle source, suggesting a feedback mechanism. We speculate that the self-sealed layer breaching stopped the connection between the deep mantle and the caldera sources as the magma injection model predicts several years of continuing uplift had the breaching not occurred (Figure 7). From a fluid mechanics point of view, this situation is analog to reservoirs that were inflating prior to an eruption and erupt with reservoir deflation and without co-eruptive magma recharge (e.g., equation 7 in (*Segall*, 2013), equation S.29 in (*Delgado et al.*, 2019)). Finally, the pattern of cyclic uplift and subsidence (Figure 1) indicates that Yellowstone might behave as a harmonic oscillator with periods of ∼10 years (e.g., (*Walwer et al.*, 2019)). More geodetic data recorded on future episodes of unrest will shed light in this aspect.

7 Conclusions

In this study we have revisited InSAR and GPS time series that span the 2004-2009 episode of ground uplift at Yellowstone caldera, the largest instrumentally detected at this volcano. Simple solid and fluid mechanics models provide for the first time quantitative evidence from geophysical data that the caldera uplift results from magma injection from a deep mantle source into a shallow source at ∼8.7 km. Magma ascent and injection only results from its overpressure, not from buoyancy effects. On the other hand, magma extraction from the NGB source towards the caldera source cannot explain the subsidence that is recorded at the former area. In general, the episode of uplift was only related to small increases in the microseismicity in areas neighboring the caldera, with no clear correlation with other instrumental observations. A more complete view of the episodes of unrest can result from a more integrated view on the different geochemical, geodetic and seismological data sets. Future studies should consider more complex mechanisms of stress-driven fluid migration, as well as a better simulation of the abrupt changes in the force balance that drive the fluid injection and extraction into the NGB and caldera sources.

Acknowledgments

F.D. acknowledges the French Centre National dEtudes Spatiales (CNES) for a post-doctoral fellowship, Charles Wicks (U.S. Geological Survey) for granting access to TSX data, Valérie Cayol (Laboratoire de Magmas et Volcanes, Université Clermont Auvergne) for her help with the DEFVOLC boundary element software and Tara Shreve (IPGP), Michael Poland, Jacob Lowenstern, Shaul Hurwitz (U.S. Geological Survey), and Juliet Biggs (University of Bristol) for discussions. The InSAR data were processed at IPGP's S-CAPAD cluster and we thank Genevieve Moguilny for her help with this computing facility.

Data Availability statement

ERS-1/2 and ENVISAT data are property of the European Space Agency (ESA) and were provided through GEO Geohazard Supersites and Natural Laboratories and UNAVCO. ALOS-1 date are property of the Japanese Ministerium of Trade and Commerce and were provided by NASA through the Alaska Satellite Facility. The TerraSAR-X data are property of Deutsche Zentrum fr Luft- und Raumfahrt (DLR) and are available at UNAVCO SSARA upon request to Principal Investigator Charles Wicks (USGS). GPS data were provided by Nevada Geodetic Laboratory and also available by the USGS Earthquake Hazard Program. Earthquakes in Figure 1 are from the USGS Earthquake Catalog.

Tables

Satellite	λ (cm)	Dates (yyyy/mm/dd)	Pass	Path	θ	Mode, Beam	#SAR	#Ifg	Atmcor	DEMcor
ENVISAT	5.56	2004/09/03 - 2010/09/17	A	48	19	IM1	26	14	no	no
ENVISAT	5.56	2004/09/22 - 2009/10/21	A	320	23	IM2	26	42	ERAW2	yes
ENVISAT	5.56	2005/05/24 - 2010/08/31	D	313	19	IM1	12	10	ERAW2	no
ENVISAT	5.56	2005/05/05 - 2010/10/21	D	41	23	IM2	28	37	ERAW2	yes
ALOS-1	23.8	2006/12/30 - 2011/02/25	A	197	38	FBD-FBS	15	7	linear	no
ALOS-1	23.8	2007/01/16 - 2011/03/14	A	198	39	FBD-FBS	19	N/A	N/A	N/A
TerraSAR-X	3.1	2011/07/23 - 2013/07/07	A	45	21	strip_003	12	2*	no	no
TerraSAR-X	3.1	2011/07/28 - 2013/10/19	A	121	35	strip_009	16	3*	no	no
TerraSAR-X	3.1	2011/07/19 - 2013/10/10	D	159	28	strip_006	10	6*	no	no

Table 1: Details of the processed SAR data sets. The columns show the satellite name, radar wavelength (λ), date range (year/month/day), whether the satellite is in an ascending (A) or descending (D) orbit, satellite path, average incidence angle (θ), radar beam except for ALOS-1 where it indicates the radar mode (either FBD or FBS, Fine Beam Double and Fine Beam Single polarization), number of synthetic aperture radar images (SAR) per track, and the number of interferograms used in the time series (Ifg). The asterisk indicates the number of stacked interferograms instead of the number pairs used in the time series inversion. Atmcor is the type of atmospheric correction applied to the data: ERAW2 atmospheric correction with the ERA5 model and an empirical correction with an elevation-dependent term on top of that. DEMcor refers to whether a DEM error correction ((*Ducret et al.*, 2014)) was used or not.

Source model	X_s (km)	Y_s (km)	Z_s (km)	L (km)	W (km)	θ	δ
Sill caldera floor	537.0**	4933.2**	8.7**	57.6**	18.6**	54*	0*
Sill NGB	528.1	4940.0	10.6	22.6	26.6	357	0*

Table 2: Best-fit sill models. X_s centroid EW coordinate, Y_s centroid NS coordinate, Z_s centroid depth, a major semi axis, b semi-minor axis. Centroid coordinates are in WGS84 UTM 12N datum. Model parameters where iteratively inverted for. First we fixed parameters with * since they converge much faster than any of the others in the NA scatterplots. After many iterations with model parameter convergence we fixed the parameters with ** . Finally we inverted the NGB model parameters .

G (GPa)	ν	H (km)	H_2 (km)	a_s (km)	a_d (km)	γ_s, γ_d	$\Delta\rho$ (kg/m^3)	V_{R_s} (km^3)	V_{R_d} (km^3)	β_m (Pa^{-1})
2.1	0.25	10	2	15	10	$\frac{8(1-\nu)}{3\pi}$	270	1000	100	0-2.1$\times10^{-10}$

Table 3: Parameters for the analytic model of magma injection connecting two reservoirs. G from (*Heap et al.*, 2020), H_2 and H from the best-fit sill inversion (Table 2), γ_s, γ_s for the crack-like sill reservoirs.

Figures

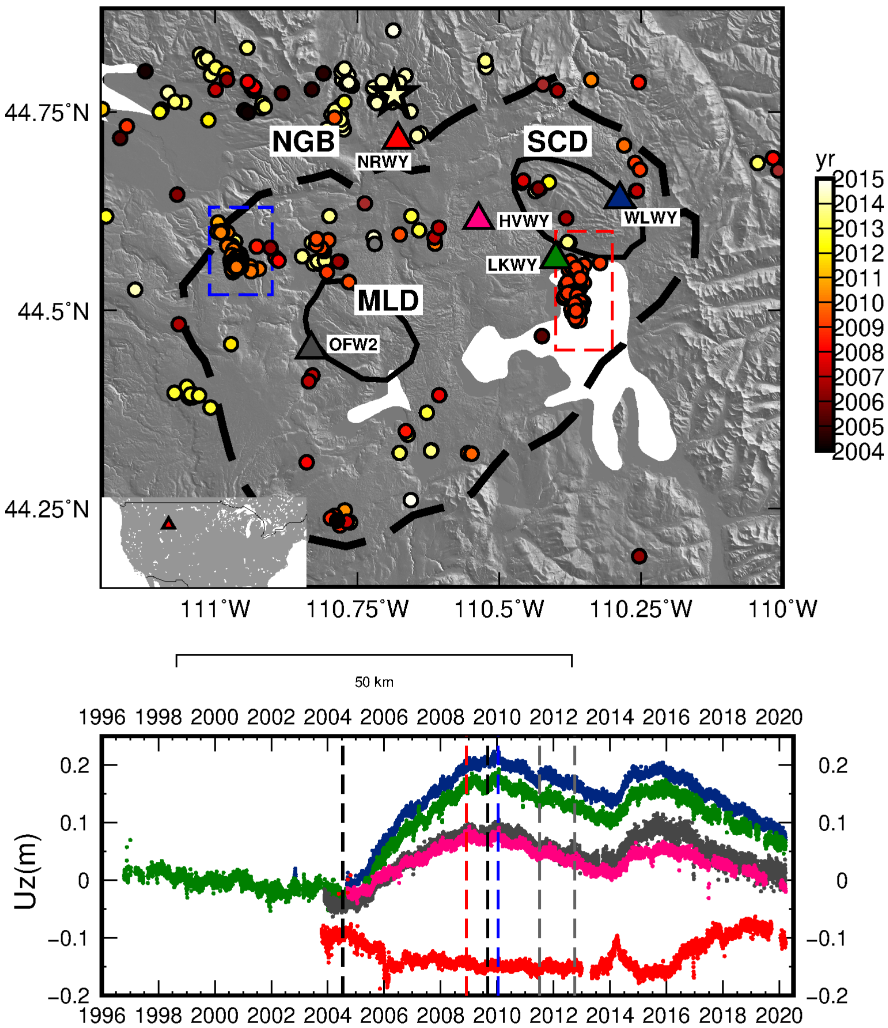

Figure 1: Top. Yellowstone caldera (thick dashed line), Mallard Lake (MLD) and Sour Creek (SCD) resurgent domes (black lines) draped over the 10m shaded NED DEM. Triangles are GPS stations that recorded data during the complete episode of unrest in 2004-2009. The dots show earthquakes from the USGS Earthquake Catalog shallower than 15 km with $M_L > 2.5$. The red and blue dashed rectangles show the December 2008 ((*Farrell et al.*, 2010)) and January 2010 Madison Plateau ((*Shelly et al.*, 2013)) seismic swarms. Inset shows location of Yellowstone caldera (red triangle) within the United States. The star is the M_W 4.8 earthquake of March 30 2014 at NGB. Bottom. GPS time series of vertical deformation (location on top). The dashed black and grey lines show the 2004-2009 episode of unrest, and the caldera subsidence covered by the TSX data during 2011-2012 respectively. The vertical red and blue lines show the December 2008 and January 2010 seismic swarms.

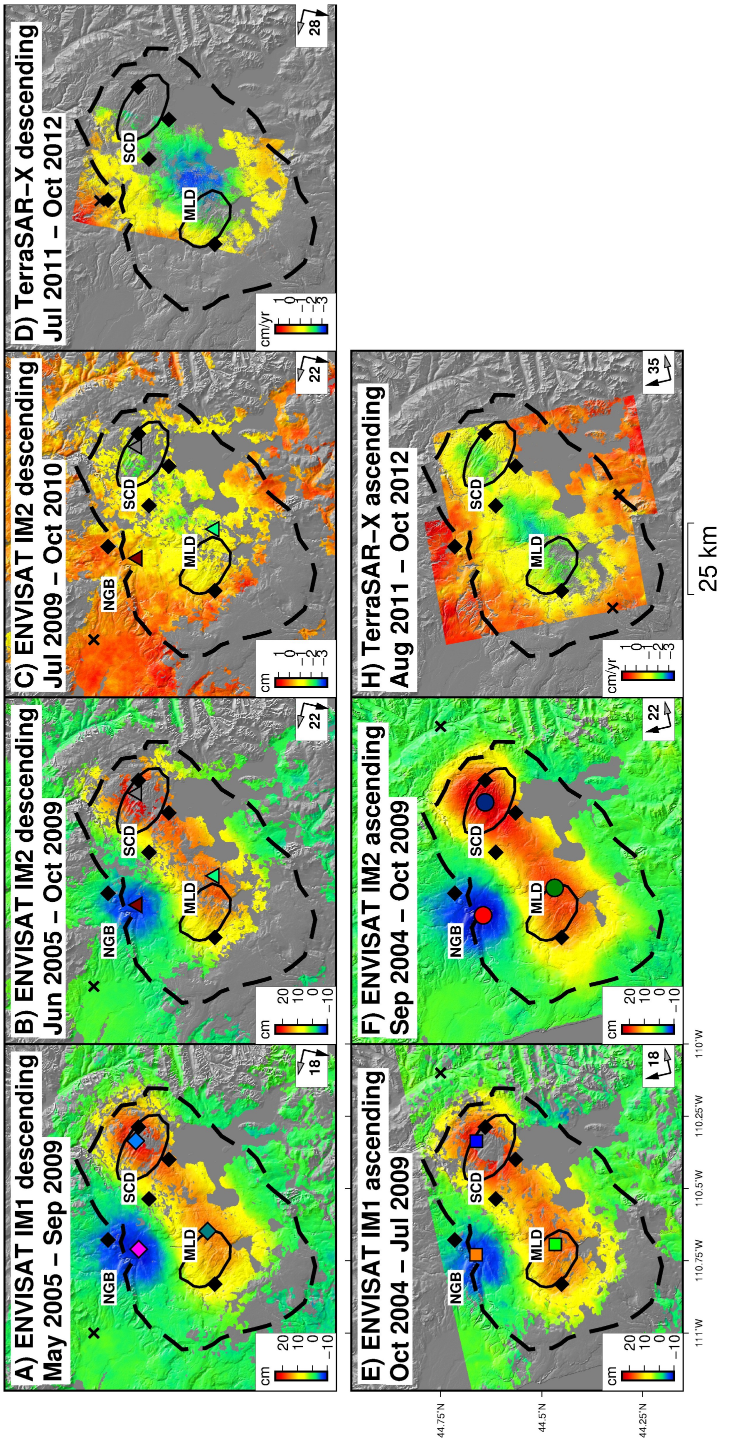

Figure 2: Mean ground velocities at Yellowstone caldera calculated for the 2004-2009 time period from InSAR time series for ENVISAT data (A, B, C, E, F), and from TSX stacks (D, G). The dashed black line is the caldera border and the thin black lines show the MLD) and (SCD). NGB is the Norris Geyser basin. The black diamonds are the continuous GPS stations used in the study (Figure 1). The color circles, squares and diamonds in (A, B, C, E, F) show the location of maximum uplift for MLD and SCD, and subsidence for NGB in the time series in Figure 2.

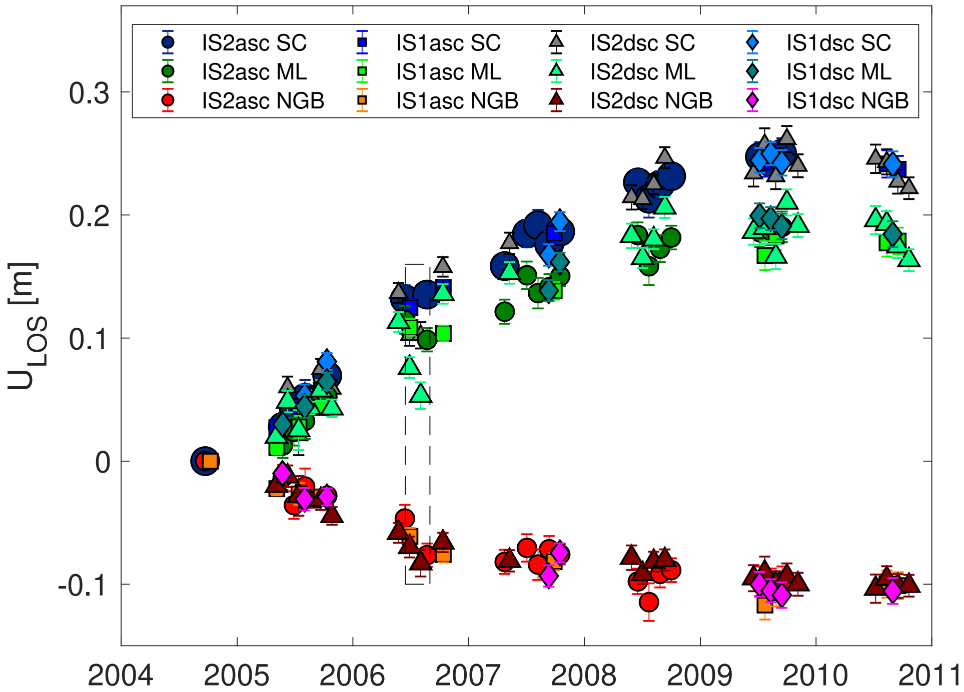

Figure 3: ENVISAT time series for selected pixels of maximum displacement at NGB, MLD SCD (Figure 2). The IM2 data show larger dispersion in the displacement because the interferograms used in the time series contain far more turbulent signals than any of the other three tracks (Supplementary Material). The dashed box show jumps in the IM2 descending time series not observed in other data sets. Using pairwise logic, these are not indicative of any ground deformation signal.

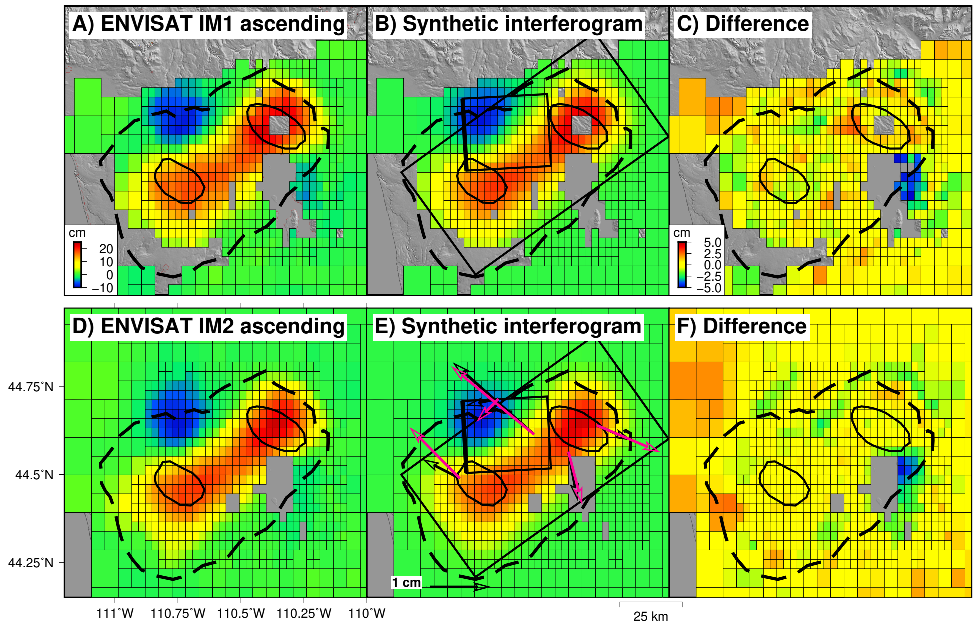

Figure 4: Downsampled (A, D), synthetic (B, E) and residual interferograms (C,F) produced by an opening sill below the caldera and by a closing sill below NG spanning 2004-2009. The black and pink arrows are the GPS data and synthetic data from the best-fit joint inversion. The rectangles are the modeled sills (Figure 5).

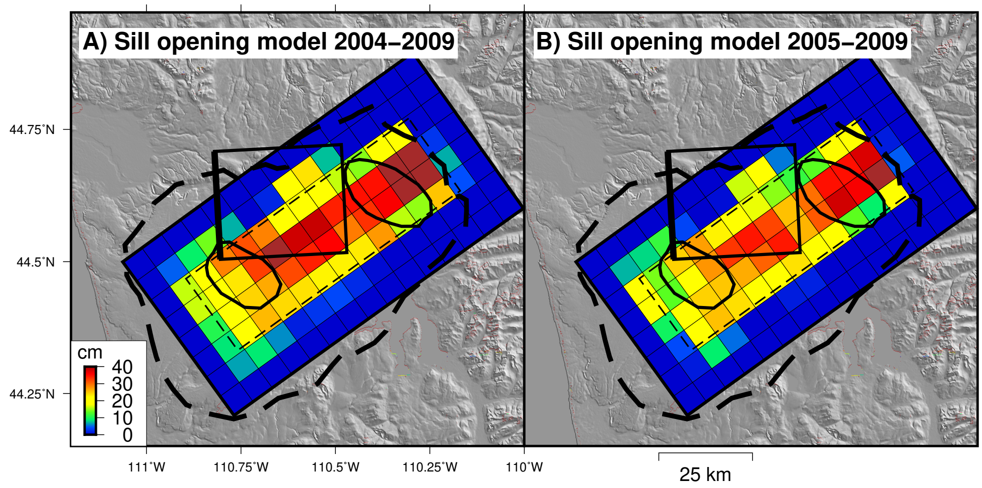

Figure 5: Distributed sill opening models for 2004-2009 (A) and 2005-2009 (B). The thin and dashed rectangles are the NGB and the caldera sources with uniform opening. The thick dashed line is the caldera border and the elliptical polygons are the SCD and MLD.

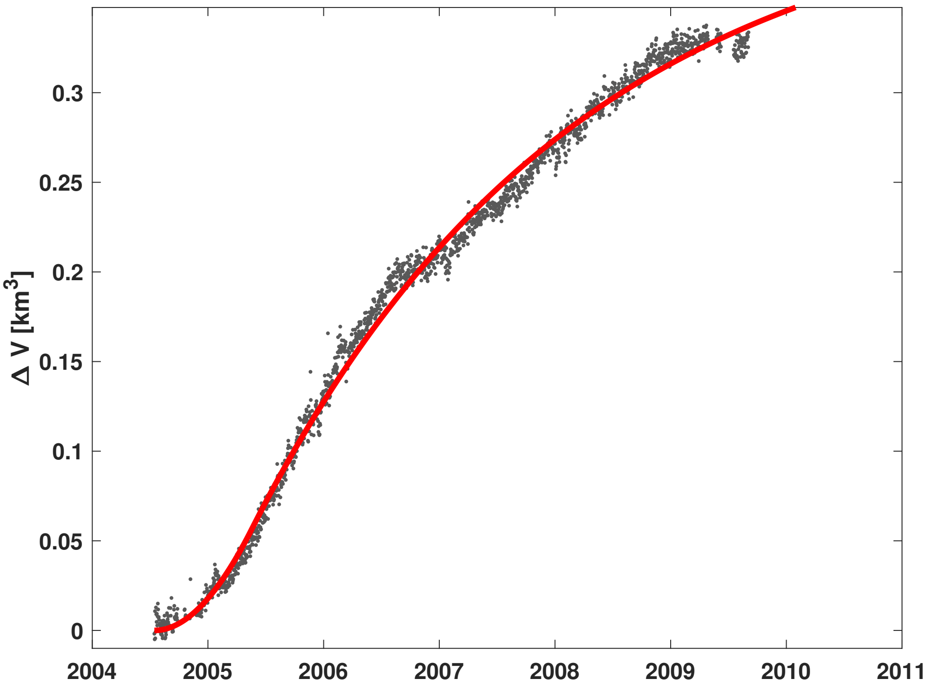

Figure 6: Time series of volume change (ΔV) for the caldera floor source with uniform opening, and inverted from the vertical component (U_z) of all the GPS stations. The red line is the best-fit Equation 1, but with P scaled to represent the source volume change.

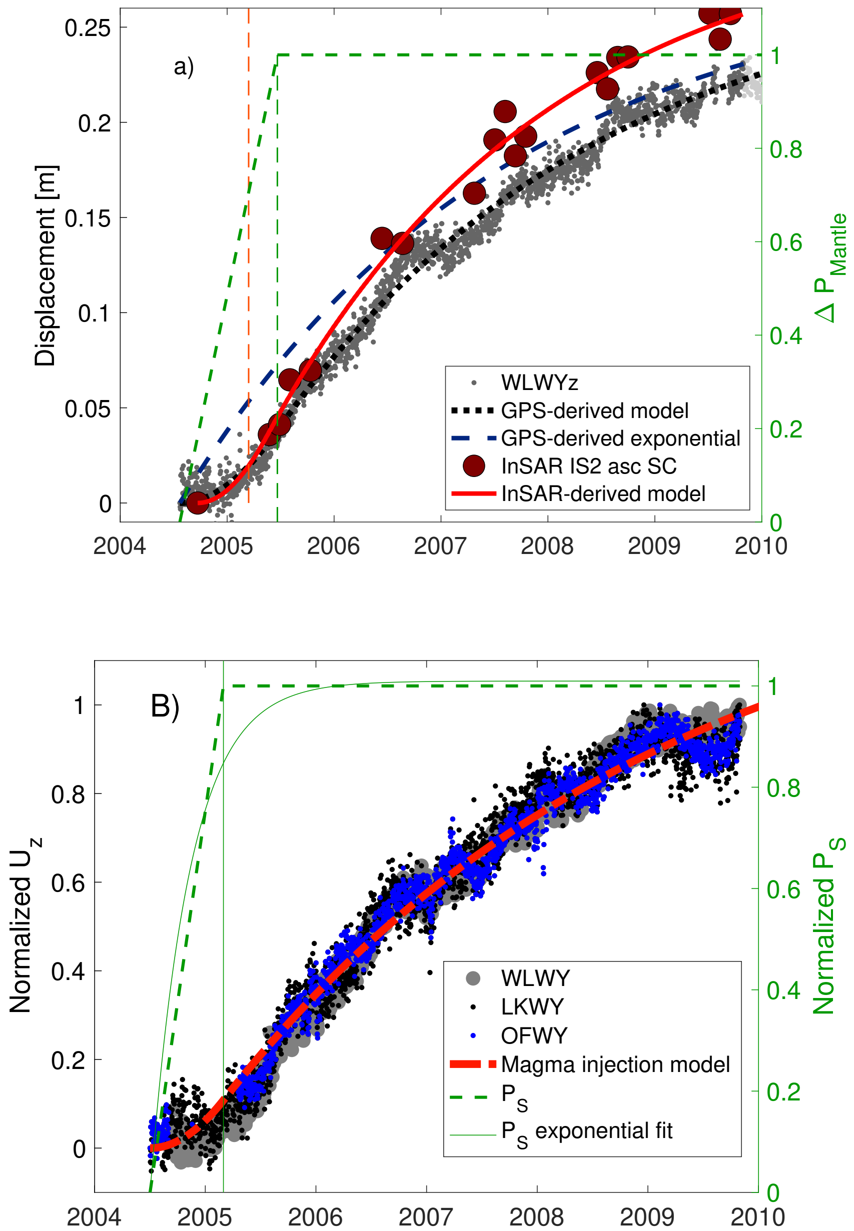

Figure 7: A. Magma injection model fits to GPS (grey dots) and InSAR (red circles) data. Displacement refers to either vertical displacement for GPS data or line-of-sight displacement for InSAR data. The red and black lines are the best-fit models to the InSAR IM2 for SCD and the vertical component of the WLWY station. The blue dashed line is the best-fit function $U = U_f(1 - e^{-t/\tau})$ with U_f the maximum displacement and τ a time constant. The vertical lines show the transition between a deep magma source with increasing pressure to a constant pressure and delimit an increasing exponential to a decreasing exponential (green line for GPS and orange line for InSAR). B. Best-fit magma injection model (red line) to the normalized vertical displacements of the WLWY, LKWY and OFW2 stations. The dashed green line is the adimensional mantle pressure function (P_s), and the green continuous line is the best-fit exponential fit of the form $P_s = P(1 - e^{-t/\tau_m})$. The latter function is used to simulate the magma flow between the caldera and NGB (Figure 10 - Figure 11).

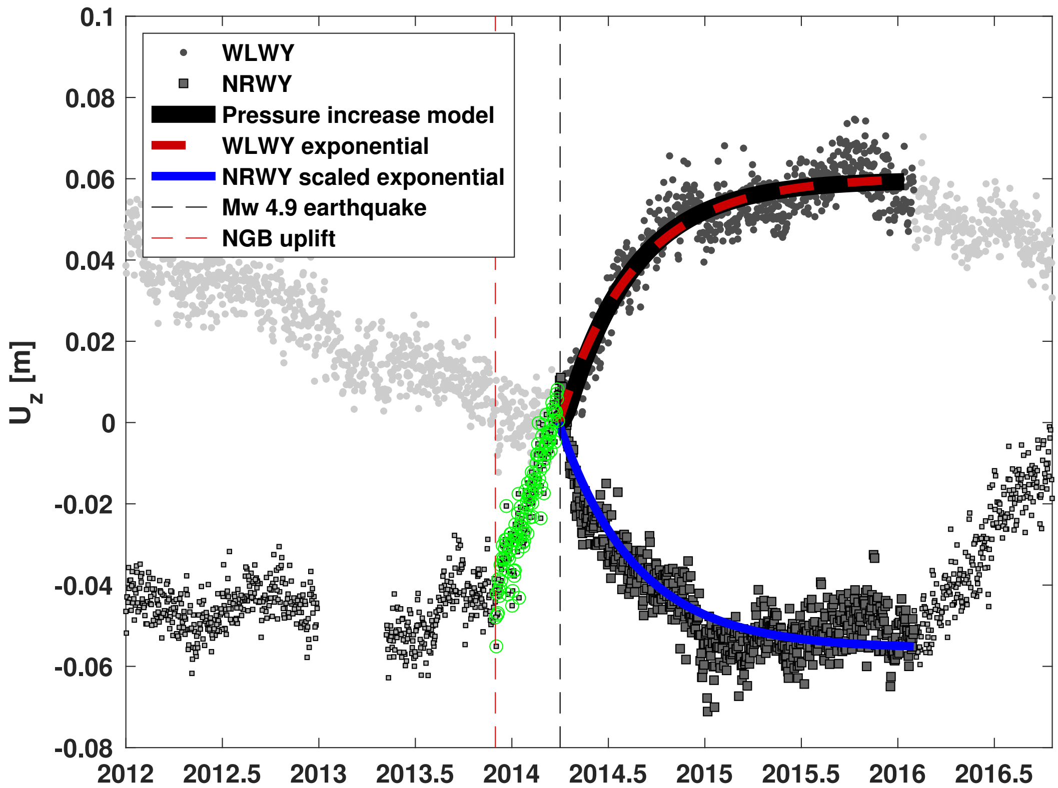

Figure 8: Time series of vertical displacement at stations WLWY and NRWY during 2014-2015, with best-fit models of magma injection for a double exponential (solid black line) and exponential fits of the form $U = U_f(1 - e^{-\frac{t}{\tau}})$ (dashed red line). The green dots show the NGB uplift during December 2013 - March 2014. The blue line is a scaled version of the exponential fit but applied to the NRWY vertical component during the same time span. The dashed vertical line shows the transition from uplift to subsidence at NGB coincident with a Mw 4.9 earthquake on March 30 2014. The model fit to the time series indicates two things. First, that the GPS data is indicative of magma injection at the caldera sill. Second, the NGB subsidence was coeval and with nearly the same time history than for the caldera sources. This conincidence was not observed during 2004-2009 (Figure 7).

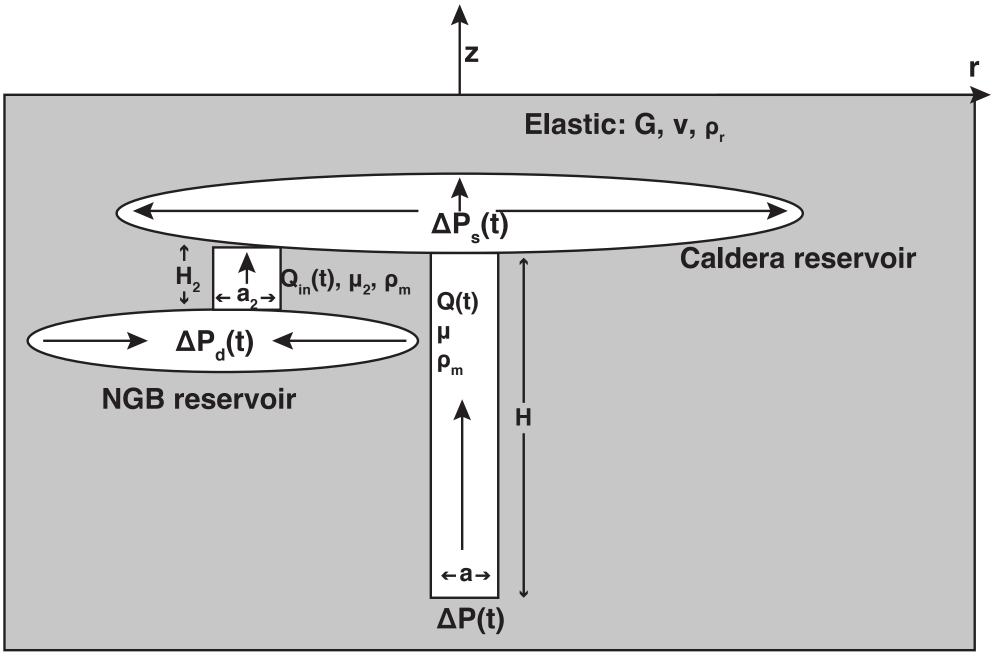

Figure 9: Sketch that shows the main physical parameters involved in the dynamic model of magma injection (Figure 10, Equation 14-Equation 15). Here P_s and P_d represent the pressure in the caldera floor and NGB reservoirs which are hydraulically connected. Magma ascends from a mantle source to the caldera source, which is also filled by magma flowing from the NGB source. The model does not consider large areas of partial melt inferred from V_P tomography ((*Farrell et al.*, 2014; *Huang et al.*, 2015)) and how the melt can either bypass or interact with these areas.

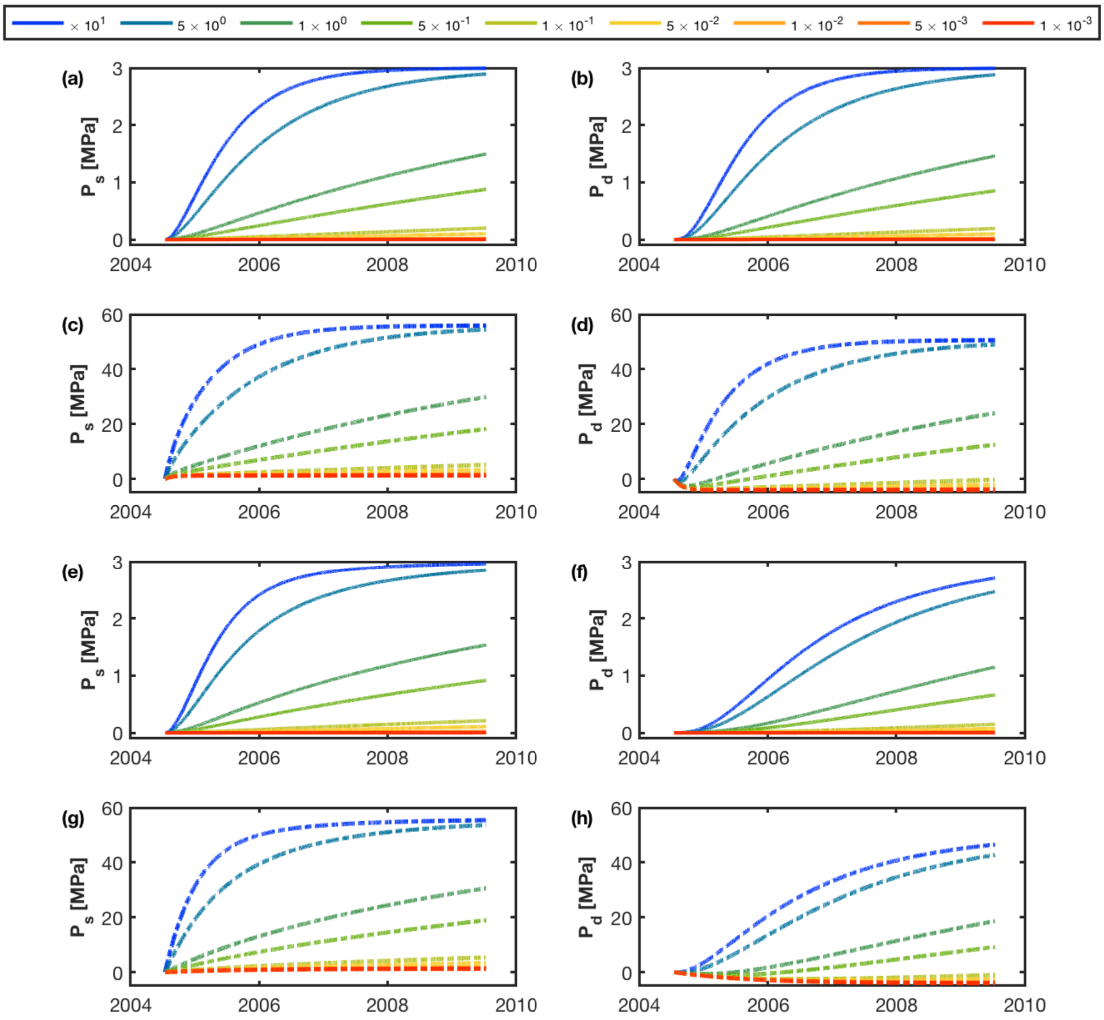

Figure 10: Simulation of the pressure change in the caldera source (P_s, a,c,e,g) and NGB (P_d, b,d,f,h) reservoirs based on the analytic model of magma transfer between the caldera floor and NGB (Equation 18) for the 2004-2009 time period. Panels a-b) show simulations with conduit flow due to magma overpressure while panels c-d) show models with flow due to both magma overpressure and buoyancy. The color lines show simulations for different conduit conductivities between the caldera sources and a deep mantle source. a-d) and e-h) show simulations for conduit conductivities of 1 and 0.1 between the caldera sill and the deeper NGB sill. Deformation due to magma injection is proportional to the source pressure change in a linear elastic half-space, so the ground deformation follows functions with the same shape than the source pressure function. The models show that magma extraction from NGB to the caldera floor cannot explain both the deformation trends observed in the GPS (Figure 1) and InSAR (Figure 3) data.

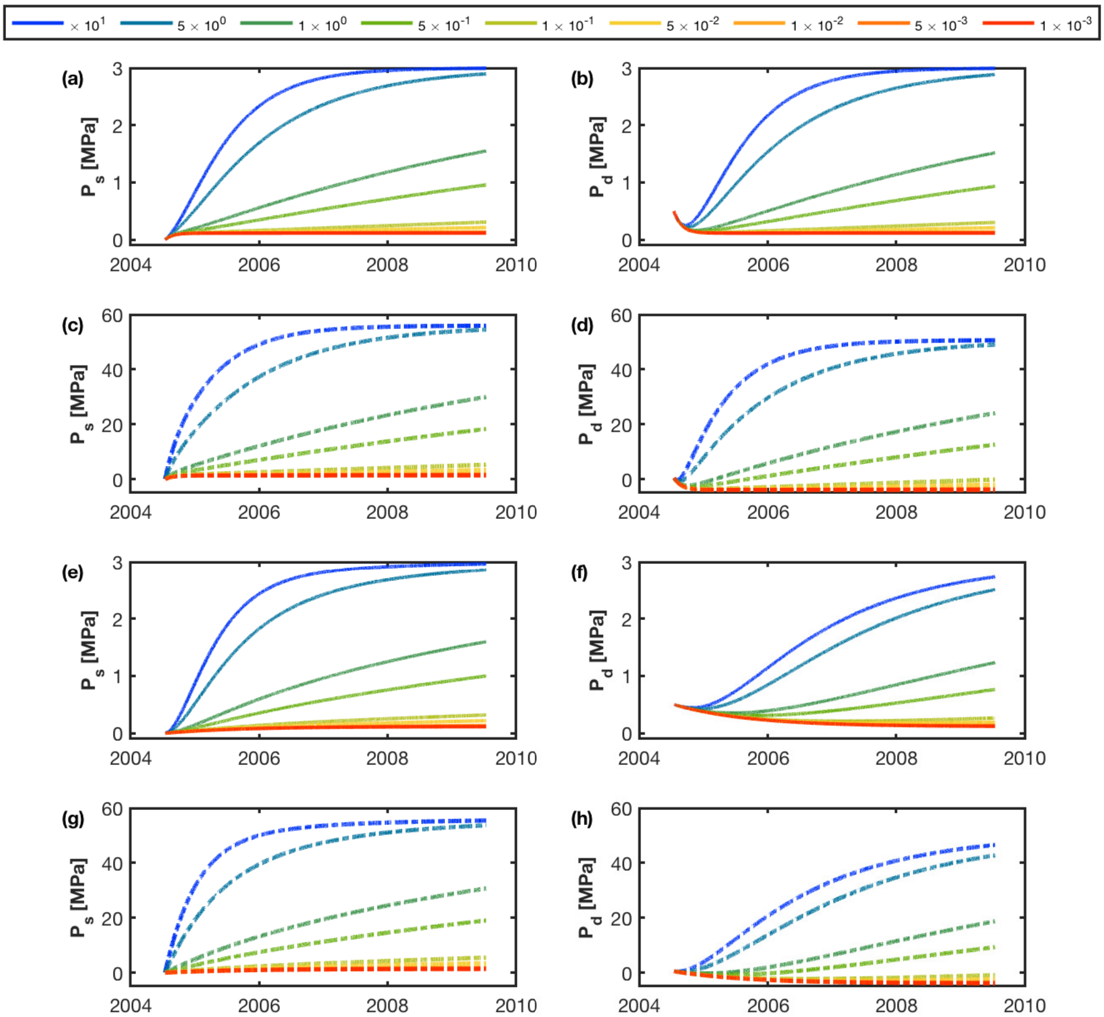

Figure 11: Same as Figure 10 but with $P_{d0} = 0.5$ MPa for the NGB sill. This simulation shows that magma extraction from NGB to the caldera can produce subsidence at NGB with a similar amplitude to that of the caldera uplift only if the NGB sill overpressure is unrealistically higher than the overpressure at the caldera sill.

References

Acocella, V. (2019), Bridging the gap from caldera unrest to resurgence, *Frontiers in Earth Science*, 10.3389/feart.2019.00173.

Albino, F., and F. Sigmundsson (2014), Stress transfer between magma bodies: Influence of intrusions prior to 2010 eruptions at Eyjafjallajokull volcano, Iceland, *Journal of Geophysical Research-Solid Earth*, *119*(4), 2964–2975, 10.1002/2013jb010510.

Albino, F., V. Pinel, and F. Sigmundsson (2010), Influence of surface load variations on eruption likelihood: application to two Icelandic subglacial volcanoes, Grimsvotn and Katla, *Geophysical Journal International*, *181*(3), 1510–1524, 10.1111/j.1365-246X.2010.04603.x.

Aly, M. H., and E. S. Cochran (2011), Spatio-temporal evolution of Yellowstone deformation between 1992 and 2009 from InSAR and GPS observations, *Bulletin of Volcanology*, 10.1007/s00445-011-0483-y.

Anderson, K., and P. Segall (2013), Bayesian inversion of data from effusive volcanic eruptions using physics-based models: Application to Mount St. Helens 2004-2008, *Journal of Geophysical Research-Solid Earth*, *118*(5), 2017–2037, 10.1002/jgrb.50169.

Annen, C. (2009), From plutons to magma chambers: Thermal constraints on the accumulation of eruptible silicic magma in the upper crust, *Earth and Planetary Science Letters*, *284*(3-4), 409–416, 10.1016/j.epsl.2009.05.006.

Annen, C., J. D. Blundy, J. Leuthold, and R. S. J. Sparks (2015), Construction and evolution of igneous bodies: Towards an integrated perspective of crustal magmatism, *Lithos*, *230*, 206–221, 10.1016/J.LITHOS.2015.05.008.

Aster, R. C., B. Borchers, and C. H. Thurber (2018), *Parameter estimation and inverse problems*, Elsevier, 10.1016/C2015-0-02458-3.

Bachmann, O., and G. Bergantz (2008), The magma reservoirs that feed supereruptions, *Elements*, *4*(1), 17–21, 10.2113/gselements.4.1.17.

Bachmann, O., and C. Huber (2016), Silicic magma reservoirs in the Earth's crust, *American Mineralogist*, *101*(11), 2377–2404, 10.2138/am-2016-5675.

Bagnardi, M., F. Amelung, and M. P. Poland (2013), A new model for the growth of basaltic shields based on deformation of Fernandina volcano, Galápagos Islands, *Earth and Planetary Science Letters*, 10.1016/j.epsl.2013.07.016.

Biggs, J., and C. Annen (2019), The lateral growth and coalesence of magma systems, *Philosophical Transactions of the Royal Society A: Mathematical, Physical and Engineering Sciences*, *377*(2139), 20180,005, 10.1098/rsta.2018.0005.

Carrier, A., J. L. Got, A. Peltier, V. Ferrazzini, T. Staudacher, P. Kowalski, and P. Boissier (2015), A damage model for volcanic edifices: Implications for edifice strength, magma pressure, and eruptive processes, *Journal of Geophysical Research: Solid Earth*, 10.1002/2014JB011485.

Cashman, K. V., R. S. J. Sparks, and J. D. Blundy (2017), Vertically extensive and unstable magmatic systems: A unified view of igneous processes, *Science*, 10.1126/science.aag3055.

Cayol, V., and F. H. Cornet (1997), 3D mixed boundary elements for elastostatic deformation field analysis, *International journal of rock mechanics and mining sciences & geomechanics abstracts*, 10.1016/S0148-9062(96)00035-6.

Chang, W.-L., R. B. Smith, C. Wicks, J. M. Farrell, and C. M. Puskas (2007), Accelerated uplift and magmatic intrusion of the Yellowstone caldera, 2004 to 2006, *Science*, *318*(5852), 952–956, 10.1126/science.1146842.

Chang, W.-L., R. B. Smith, J. Farrell, and C. M. Puskas (2010), An extraordinary episode of Yellowstone caldera uplift, 2004-2010, from GPS and InSAR observations, *Geophysical Research Letters*, *37*, 10.1029/2010gl045451.

Christiansen, R. L. (2001), The Quaternary and Pliocene Yellowstone Plateau volcanic field of Wyoming, Idaho, and Montana, *US Geological Survey Professional Paper*, 10.3133/pp729G.

Cooper, K. M. (2017), What Does a Magma Reservoir Look Like? The "Crystal's-Eye" View, *Elements*, *13*(1), 23–28, 10.2113/gselements.13.1.23.

Cooper, K. M., and A. J. Kent (2014), Rapid remobilization of magmatic crystals kept in cold storage, *Nature*, 10.1038/nature12991.

D'Auria, L., S. Pepe, R. Castaldo, F. Giudicepietro, G. Macedonio, P. Ricciolino, P. Tizzani, F. Casu, R. Lanari, M. Manzo, M. Martini, E. Sansosti, and I. Zinno (2015), Magma injection beneath the urban area of Naples: A new mechanism for the 2012-2013 volcanic unrest at Campi Flegrei caldera, *Scientific Reports*, 10.1038/srep13100.

Davidge, L., C. Ebinger, M. Ruiz, G. Tepp, F. Amelung, D. Geist, D. Coté, and J. Anzieta (2017), Seismicity patterns during a period of inflation at Sierra Negra volcano, Galápagos Ocean Island Chain, *Earth and Planetary Science Letters*, 10.1016/j.epsl.2016.12.021.

de Zeeuw-van Dalfsen, E., H. Rymer, E. Sturkell, R. Pedersen, A. Hooper, F. Sigmundsson, and B. Ófeigsson (2013), Geodetic data shed light on ongoing caldera subsidence at Askja, Iceland, *Bulletin of Volcanology*, 10.1007/s00445-013-0709-2.

Degruyter, W., and C. Huber (2014), A model for eruption frequency of upper crustal silicic magma chambers, *Earth and Planetary Science Letters*, *403*, 117–130, 10.1016/j.epsl.2014.06.047.

Delgado, F. (2020), Rhyolitic volcano dynamics in the Southern Andes: Contributions from 17 years of InSAR observations at Cordón Caulle from 2003 to 2020, *Journal of South American Earth Sciences*, 10.1016/j.jsames.2020.102841.

Delgado, F., M. E. Pritchard, D. Basualto, J. Lazo, L. Cordova, and L. E. Lara (2016), Rapid reinflation following the 2011-2012 rhyodacite eruption at Cordon Caulle volcano (Southern Andes) imaged by InSAR: Evidence for magma reservoir refill, *Geophysical Research Letters*, *43*(18), 9552–9562, 10.1002/2016gl070066.

Delgado, F., M. Pritchard, S. Samsonov, and L. Córdova (2018), Renewed post-eruptive uplift following the 2011-2012 rhyolitic eruption of Cordón Caulle (Southern Andes, Chile): evidence for transient episodes of magma reservoir recharge during 2012-2018, *Journal of Geophysical Research: Solid Earth*, 10.1029/2018JB016240.

Delgado, F., J. Kubanek, K. Anderson, P. Lundgren, and M. Pritchard (2019), Physicochemical models of effusive rhyolitic eruptions constrained with InSAR and DEM data: A case study of the 2011-2012 Cordón Caulle eruption, *Earth and Planetary Science Letters*, *524*, 115,736, 10.1016/J.EPSL.2019.115736.

Doin, M.-P., F. Lodge, S. Guillaso, R. Jolivet, C. Lasserre, G. Ducret, R. Grandin, E. Pathier, and V. Pinel (2011), Presentation of the small baseline NSBAS processing chain on a case example: the Etna deformation monitoring from 2003 to 2010 using Envisat data, in *Proceedings of the ESA Fringe Workshop*.

Druitt, T. H., D. M. Pyle, and T. A. Mather (2019), Santorini volcano and its plumbing system, *Elements*, 10.2138/gselements.15.3.177.

Ducret, G., M.-P. Doin, R. Grandin, C. Lasserre, and S. Guillaso (2014), DEM Corrections Before Unwrapping in a Small Baseline Strategy for InSAR Time Series Analysis, *Ieee Geoscience and Remote Sensing Letters*, *11*(3), 696–700, 10.1109/lgrs.2013.2276040.

Dvorak, J. J., and G. Berrino (1991), Recent ground movenet and seismic activity in Campi Flegrei, southern Italy: episodic growth of a resurgent dome, *Journal of Geophysical Research-Solid Earth and Planets*, *96*(B2), 2309–2323, 10.1029/90jb02225.

Dzurisin, D., and Z. Lu (2007), Interferometric synthetic-aperture radar (InSAR), in *Volcano Deformation*, edited by D. Dzurisin, chap. 5, pp. 153–194, Springer, Berlin, Heidelberg, 10.1007/978-3-540-49302-0_5.

Dzurisin, D., J. C. Savage, and R. O. Fournier (1990), Recent crustal subsidence at Yellowstone Caldera, Wyoming, *Bulletin of Volcanology*, 10.1007/BF00304098.

Dzurisin, D., C. Wicks, and W. Thatcher (1999), Renewed uplift at the Yellowstone caldera measured by leveling surveys and satellite radar interferometry, *Bulletin of Volcanology*, 10.1007/s004450050277.

Dzurisin, D., C. W. Wicks, and M. P. Poland (2012), History of surface displacements at the Yellowstone Caldera, Wyoming, from leveling surveys and InSAR observations, 19232008, *U.S. Geological Survey Professional Paper*, *1788*, 68 p.

Dzurisin, D., Z. Lu, M. P. Poland, and C. W. Wicks (2019), Space-Based Imaging Radar Studies of U.S. Volcanoes, *Frontiers in Earth Science*, *6*, 249, 10.3389/feart.2018.00249.

Evans, W. C., D. Bergfeld, M. C. van Soest, M. A. Huebner, J. Fitzpatrick, and K. M. Revesz (2006), Geochemistry of low-temperature springs northwest of Yellowstone caldera: Seeking the link between seismicity, deformation, and fluid flow, *Journal of Volcanology and Geothermal Research*, 10.1016/j.jvolgeores.2006.01.001.

Farrell, J. (2014), Seismicity and tomographic imaging of the Yellowstone crustal magmatic-tectonic system, Ph.D. thesis, University of Utah.

Farrell, J., S. Husen, and R. B. Smith (2009), Earthquake swarm and b-value characterization of the Yellowstone volcano-tectonic system, *Journal of Volcanology and Geothermal Research*, 10.1016/j.jvolgeores.2009.08.008.

Farrell, J., R. B. Smith, T. Taira, W.-L. Chang, and C. M. Puskas (2010), Dynamics and rapid migration of the energetic 2008-2009 Yellowstone Lake earthquake swarm, *Geophysical Research Letters*, *37*(19), n/a–n/a, 10.1029/2010GL044605.

Farrell, J., R. B. Smith, S. Husen, and T. Diehl (2014), Tomography from 26years of seismicity revealing that the spatial extent of the Yellowstone crustal magma reservoir extends well beyond the Yellowstone caldera, *Geophysical Research Letters*, 10.1002/2014GL059588.

Feigl, K. L., H. Le Mével, S. T. Ali, L. Cordova, N. L. Andersen, C. DeMets, and B. S. Singer (2014), Rapid uplift in Laguna del Maule volcanic field of the Andean Southern Volcanic zone (Chile) 2007-2012, *Geophysical Journal International*, *196*(2), 885–901, 10.1093/gji/ggt438.

Fialko, Y. (2004), Evidence of fluid-filled upper crust from observations of postseismic deformation due to the 1992 Mw7.3 Landers earthquake, *Journal of Geophysical Research: Solid Earth*, 10.1029/2004JB002985.

Fialko, Y., M. Simons, and Y. Khazan (2001a), Finite source modelling of magmatic unrest in Socorro, New Mexico, and Long Valley, California, *Geophysical Journal International*, 10.1046/j.1365-246X.2001.00453.x.

Fialko, Y., Y. Khazan, and M. Simons (2001b), Deformation due to a pressurized horizontal circular crack in an elastic half-space, with applications to volcano geodesy, *Geophysical Journal International*, *146*(1), 181–190, 10.1046/j.1365-246X.2001.00452.x.

Fournier, R. O. (1989), Geochemistry and dynamics of the Yellowstone National Park hydrothermal system, *Annual review of earth and planetary sciences. Vol. 17*, 10.1146/annurev.earth.17.1.13.

Fournier, R. O. (2007), Hydrothermal systems and volcano geochemistry, in *Volcano Deformation*, edited by D. Dzurisin, chap. 10, pp. 323–341, Springer, Berlin, Heidelberg, 10.1007/978-3-540-49302-0_10.

Fukushima, Y., V. Cayol, P. Durand, and D. Massonnet (2010), Evolution of magma conduits during the 1998-2000 eruptions of Piton de la Fournaise volcano, Reunion Island, *Journal of Geophysical Research-Solid Earth*, *115*, 10.1029/2009jb007023.

Giordano, D., and D. B. Dingwell (2003), Non-Arrhenian multicomponent melt viscosity: A model, *Earth and Planetary Science Letters*, 10.1016/S0012-821X(03)00042-6.

Giudicepietro, F., G. Macedonio, and M. Martini (2017), A Physical Model of Sill Expansion to Explain the Dynamics of Unrest at Calderas with Application to Campi Flegrei, *Frontiers in Earth Science*, *5*(54), 10.3389/feart.2017.00054.

Heap, M. J., M. Villeneuve, F. Albino, J. I. Farquharson, E. Brothelande, F. Amelung, J. L. Got, and P. Baud (2020), Towards more realistic values of elastic moduli for volcano modelling, *Journal of Volcanology and Geothermal Research*, 10.1016/j.jvolgeores.2019.106684.

Heimisson, E. R., P. Einarsson, F. Sigmundsson, and B. Brandsdottir (2015), Kilometer-scale Kaiser effect identified in Krafla volcano, Iceland, *Geophysical Research Letters*, *42*(19), 7958–7965, 10.1002/2015gl065680.

Henderson, S. T., F. Delgado, J. Elliott, M. E. Pritchard, and P. R. Lundgren (2017), Decelerating uplift at Lazufre volcanic center, Central Andes, from A.D. 2010 to 2016, and implications for geodetic models, *Geosphere*, 10.1130/GES01441.1.

Hildreth, W. (2017), Fluid-driven uplift at Long Valley Caldera, California: Geologic perspectives, *Journal of Volcanology and Geothermal Research*, *341*, 269–286, 10.1016/j.jvolgeores.2017.06.010.

Hill, D., E. Montgomery-Brown, D. R. Shelly, A. Flinders, and S. Prejean (2020), Post-1978 Tumescence at Long Valley Caldera, California: a Geophysical Perspective, *Journal of Volcanology and Geothermal Research*, 10.1016/j.jvolgeores.2020.106900.

Huang, H. H., F. C. Lin, B. Schmandt, J. Farrell, R. B. Smith, and V. C. Tsai (2015), The Yellowstone magmatic system from the mantle plume to the upper crust, *Science*, 10.1126/science.aaa5648.

Huber, C., O. Bachmann, and J. Dufek (2010), The limitations of melting on the reactivation of silicic mushes, *Journal of Volcanology and Geothermal Research*, 10.1016/j.jvolgeores.2010.06.006.

Huber, C., O. Bachmann, and J. Dufek (2011), Thermo-mechanical reactivation of locked crystal mushes: Melting-induced internal fracturing and assimilation processes in magmas, *Earth and Planetary Science Letters*, 10.1016/j.epsl.2011.02.022.

Huber, C., O. Bachmann, and J. Dufek (2012), Crystal-poor versus crystal-rich ignimbrites: A competition between stirring and reactivation, *Geology*, 10.1130/G32425.1.

Hurwitz, S., and J. B. Lowenstern (2014), Dynamics of the Yellowstone hydrothermal system, *Reviews of Geophysics*, *52*(3), 375–411, 10.1002/2014rg000452.

Hurwitz, S., and M. Manga (2017), The Fascinating and Complex Dynamics of Geyser Eruptions, *Annual Review of Earth and Planetary Sciences*, 10.1146/annurev-earth-063016-015605.

Hurwitz, S., L. B. Christiansen, and P. A. Hsieh (2007a), Hydrothermal fluid flow and deformation in large calderas: Inferences from numerical simulations, *Journal of Geophysical Research-Solid Earth*, *112*(B2), 10.1029/2006jb004689.

Hurwitz, S., J. B. Lowenstern, and H. Heasler (2007b), Spatial and temporal geochemical trends in the hydrothermal system of Yellowstone National Park: Inferences from river solute fluxes, *Journal of Volcanology and Geothermal Research*, 10.1016/j.jvolgeores.2007.01.003.

Hurwitz, S., W. C. Evans, and J. B. Lowenstern (2010), River solute fluxes reflecting active hydrothermal chemical weathering of the Yellowstone Plateau Volcanic Field, USA, *Chemical Geology*, 10.1016/j.chemgeo.2010.07.001.

Hurwitz, S., A. G. Hunt, and W. C. Evans (2012), Temporal variations of geyser water chemistry in the Upper Geyser Basin, Yellowstone National Park, USA, *Geochemistry, Geophysics, Geosystems*, 10.1029/2012GC004388.

Jaupart, C., and S. Tait (1990), Dynamics of eruptive phenomena, *Reviews in Mineralogy*, *24*, 213–238.

Jay, J., F. Costa, M. Pritchard, L. Lara, B. Singer, and J. Herrin (2014), Locating magma reservoirs using InSAR and petrology before and during the 2011-2012 Cordon Caulle silicic eruption, *Earth and Planetary Science Letters*, *403*, 463, 10.1016/j.epsl.2014.07.021.

Jellinek, A. M., and D. J. DePaolo (2003), A model for the origin of large silicic magma chambers: precursors of caldera-forming eruptions, *Bulletin of Volcanology*, *65*(5), 363–381, 10.1007/s00445-003-0277-y.

Le Mével, H., K. L. Feigl, L. Córdova, C. DeMets, and P. Lundgren (2015), Evolution of unrest at Laguna del Maule volcanic field (Chile) from InSAR and GPS measurements, 2003 to 2014, *Geophysical Research Letters*, *42*(16), 6590–6598, 10.1002/2015GL064665.

Le Mével, H., P. Gregg, and K. L. Feigl (2016), Magma injection into a long-lived reservoir to explain geodetically measured uplift: application to the 20072014 unrest episode at Laguna del Maule volcanic field, Chile, *Journal of Geophysical Research: Solid Earth*, pp. n/a–n/a, 10.1002/2016JB013066.

Lengline, O., D. Marsan, J. L. Got, V. Pinel, V. Ferrazzini, and P. G. Okubo (2008), Seismicity and deformation induced by magma accumulation at three basaltic volcanoes, *Journal of Geophysical Research-Solid Earth*, *113*(B12), 12, 10.1029/2008jb005937.

Lewicki, J. L., P. J. Kelly, D. Bergfeld, R. G. Vaughan, and J. B. Lowenstern (2017), Monitoring gas and heat emissions at Norris Geyser Basin, Yellowstone National Park, USA based on a combined eddy covariance and Multi-GAS approach, *Journal of Volcanology and Geothermal Research*, 10.1016/j.jvolgeores.2017.10.001.

Liu, Z., D. Dong, and P. Lundgren (2011), Constraints on time-dependent volcanic source models at Long Valley Caldera from 1996 to 2009 using InSAR and geodetic measurements, *Geophysical Journal International*, *187*(3), 1283–1300, 10.1111/j.1365-246X.2011.05214.x.

Lohman, R. B., and M. Simons (2005), Some thoughts on the use of InSAR data to constrain models of surface deformation: Noise structure and data downsampling, *Geochemistry Geophysics Geosystems*, *6*, 12, 10.1029/2004gc000841.

Lowenstern, J. B., and S. Hurwitz (2008), Monitoring a supervolcano in repose: Heat and volatile flux at the yellostone caldera, *Elements*, 10.2113/GSELEMENTS.4.1.35.

Lowenstern, J. B., D. Bergfeld, W. C. Evans, and A. G. Hunt (2015), Origins of geothermal gases at Yellowstone, 10.1016/j.jvolgeores.2015.06.010.

Lowenstern, J. B., T. W. Sisson, and S. Hurwitz (2017), Probing magma reservoirs to improve volcano forecasts, *EOS*, *98*, doi.org/10.1029/2017EO085189.

Lu, Z., and D. Dzurisin (2010), Ground surface deformation patterns, magma supply, and magma storage at Okmok volcano, Alaska, from InSAR analysis: 2. Coeruptive deflation, July-August 2008, *Journal of Geophysical Research-Solid Earth*, *115*, 10.1029/2009jb006970.

Lu, Z., T. Masterlark, D. Dzurisin, R. Rykhus, and C. Wicks (2003), Magma supply dynamics at Westdahl volcano, Alaska, modeled from satellite radar interferometry, *Journal of Geophysical Research-Solid Earth*, *108*(B7), 10.1029/2002jb002311.

Lu, Z., D. Dzurisin, J. Biggs, C. Wicks, and S. McNutt (2010), Ground surface deformation patterns, magma supply, and magma storage at Okmok volcano, Alaska, from InSAR analysis: 1. Intereruption deformation, 1997-2008, *Journal of Geophysical Research-Solid Earth*, *115*, 10.1029/2009jb006969.

Lundgren, P., S. Usai, E. Sansosti, R. Lanari, M. Tesauro, G. Fornaro, and P. Berardino (2001), Modeling surface deformation observed with synthetic aperture radar interferometry at Campi Flegrei caldera, *Journal of Geophysical Research: Solid Earth*, *106*(B9), 19,355–19,366, 10.1029/2001JB000194.

Manga, M., I. Beresnev, E. E. Brodsky, J. E. Elkhoury, D. Elsworth, S. E. Ingebritsen, D. C. Mays, and C. Y. Wang (2012), Changes in permeability caused by transient stresses: Field observations, experiments, and mechanisms, *Reviews of Geophysics*, 10.1029/2011RG000382.

McTigue, D. F. (1987), Elastic stress and deformation near a finite spherical magma body: Resolution of the point source paradox, *Journal of Geophysical Research: Solid Earth*, *92*(B12), 12,931–12,940, 10.1029/JB092iB12p12931.

Miller, C. A., H. Le Mevel, G. Currenti, G. Williams-Jones, and B. Tikoff (2017), Microgravity changes at the Laguna del Maule volcanic field: Magma-induced stress changes facilitate mass addition, *Journal of Geophysical Research-Solid Earth*, *122*(4), 3179–3196, 10.1002/2017jb014048.

Miller, C. F., and D. A. Wark (2008), Supervolcanoes and their explosive supereruptions, *Elements*, *4*(1), 11–15, 10.2113/gselements.4.1.11.

Montgomery-Brown, E. K., C. W. Wicks, P. F. Cervelli, J. O. Langbein, J. L. Svarc, D. R. Shelly, D. P. Hill, and M. Lisowski (2015), Renewed inflation of Long Valley Caldera, California (2011 to 2014), *Geophysical Research Letters*, *42*(13), 5250–5257, 10.1002/2015gl064338.

Okada, Y. (1985), Surface deformation due to shear and tensile faullts in a half-space, *Bulletin of the Seismological Society of America*, *75*(4), 1135–1154.

Parks, M. M., J. Biggs, P. England, T. A. Mather, P. Nomikou, K. Palamartchouk, X. Papanikolaou, D. Paradissis, B. E. Parsons, D. M. Pyle, C. Raptakis, and V. Zacharis (2012), Evolution of Santorini Volcano dominated by episodic and rapid fluxes of melt from depth, *Nature Geoscience*, *5*(10), 749–754, 10.1038/ngeo1562.

Pascal, K., J. Neuberg, and E. Rivalta (2014), On precisely modelling surface deformation due to interacting magma chambers and dykes, *Geophysical Journal International*, *196*(1), 253–278, 10.1093/gji/ggt343.

Pedersen, R., and F. Sigmundsson (2006), Temporal development of the 1999 intrusive episode in the Eyjafjallajokull volcano, Iceland, derived from InSAR images, *Bulletin of Volcanology*, *68*(4), 377–393, 10.1007/s00445-005-0020-y.

Pelton, J. R., and R. B. Smith (1979), Recent crustal uplift in Yellowstone National Park, *Science*, 10.1126/science.206.4423.1179.

Pierce, K. L., K. P. Cannon, G. A. Meyer, M. J. Trebesch, and R. D. Watts (2002), Post-Glacial Inflation-Deflation Cycles, Tilting, and Faulting in the Yellowstone Caldera Based on Yellowstone Lake Shorelines Open-File Report 02-0142, *US Geological Survey Professional Paper*.

Pinel, V., and C. Jaupart (2003), Magma chamber behavior beneath a volcanic edifice, *Journal of Geophysical Research-Solid Earth*, *108*(B2), 10.1029/2002jb001751.

Pinel, V., C. Jaupart, and F. Albino (2010), On the relationship between cycles of eruptive activity and growth of a volcanic edifice, *Journal of Volcanology and Geothermal Research*, *194*(4), 150–164, 10.1016/j.jvolgeores.2010.05.006.

Poland, M., R. Bürgmann, D. Dzurisin, M. Lisowski, T. Masterlark, S. Owen, and J. Fink (2006), Constraints on the mechanism of long-term, steady subsidence at Medicine Lake volcano, northern California, from GPS, leveling, and InSAR, *Journal of Volcanology and Geothermal Research*, 10.1016/j.jvolgeores.2005.07.007.

Poland, M. P., and E. Zeeuwvan Dalfsen (2019), Assessing Seasonal Changes in Microgravity at Yellowstone Caldera, *Journal of Geophysical Research: Solid Earth*, p. 2018JB017061, 10.1029/2018JB017061.

Pritchard, M. E., and M. Simons (2004), An InSAR-based survey of volcanic deformation in the southern Andes, *Geophysical Research Letters*, *31*(15), 4, 10.1029/2004gl020545.

Pritchard, M. E., T. A. Mather, S. R. McNutt, F. J. Delgado, and K. Reath (2019), Thoughts on the criteria to determine the origin of volcanic unrest as magmatic or non-magmatic, *Philosophical Transactions of the Royal Society A: Mathematical, Physical and Engineering Sciences*, *377*(2139), 20180,008, 10.1098/rsta.2018.0008.

Reverso, T., J. Vandemeulebrouck, F. Jouanne, V. Pinel, T. Villemin, E. Sturkell, and P. Bascou (2014), A two-magma chamber model as a source of deformation at Grimsvotn Volcano, Iceland, *Journal of Geophysical Research-Solid Earth*, *119*(6), 4666–4683, 10.1002/2013jb010569.

Rivalta, E. (2010), Evidence that coupling to magma chambers controls the volume history and velocity of laterally propagating intrusions, *Journal of Geophysical Research: Solid Earth*, 10.1029/2009JB006922.

Rubin, A. E., K. M. Cooper, C. B. Till, A. J. Kent, F. Costa, M. Bose, D. Gravley, C. Deering, and J. Cole (2017), Rapid cooling and cold storage in a silicic magma reservoir recorded in individual crystals, *Science*, 10.1126/science.aam8720.

Russo, E., G. Waite, and A. Tibaldi (2017), Evaluation of the evolving stress field of the Yellowstone volcanic plateau, 1988 to 2010, from earthquake first-motion inversions, *Tectonophysics*, *700-701*, 80–91, 10.1016/J.TECTO.2017.02.009.

Sambridge, M. (1999), Geophysical inversion with a neighbourhood algorithm - I. Searching a parameter space, *Geophysical Journal International*, *138*(2), 479–494, 10.1046/j.1365-246X.1999.00876.x.

Schmandt, B., C. Jiang, and J. Farrell (2019), Seismic perspectives from the western U.S. on magma reservoirs underlying large silicic calderas, 10.1016/j.jvolgeores.2019.07.015.

Segall, P. (2013), Volcano deformation and eruption forecasting, *Remote Sensing of Volcanoes and Volcanic Processes: Integrating Observation and Modelling*, *380*, 85–106, 10.1144/sp380.4.

Segall, P. (2019), Magma chambers: What we can, and cannot, learn from volcano geodesy, 10.1098/rsta.2018.0158.

Shelly, D. R., D. P. Hill, F. Massin, J. Farrell, R. B. Smith, and T. Taira (2013), A fluid-driven earthquake swarm on the margin of the Yellowstone caldera, *Journal of Geophysical Research E: Planets*, 10.1002/jgrb.50362.

Sigmundsson, F., S. Hreinsdottir, A. Hooper, T. Arnadottir, R. Pedersen, M. J. Roberts, N. Oskarsson, A. Auriac, J. Decriem, P. Einarsson, H. Geirsson, M. Hensch, B. G. Ofeigsson, E. Sturkell, H. Sveinbjornsson, and K. L. Feigl (2010), Intrusion triggering of the 2010 Eyjafjallajokull explosive eruption, *Nature*, *468*(7322), 426–U253, 10.1038/nature09558.

Sparks, R. S. J., and K. V. Cashman (2017), Dynamic Magma Systems: Implications for Forecasting Volcanic Activity, *Elements*, *13*(1), 35–40, 10.2113/gselements.13.1.35.

Sparks, R. S. J., C. Annen, J. D. Blundy, K. V. Cashman, A. C. Rust, and M. D. Jackson (2019), Formation and dynamics of magma reservoirs, *Philosophical Transactions of the Royal Society A: Mathematical, Physical and Engineering Sciences*, *377*(2139), 20180,019, 10.1098/rsta.2018.0019.

Taira, T., R. B. Smith, and W. L. Chang (2010), Seismic evidence for dilatational source deformations accompanying the 2004-2008 Yellowstone accelerated uplift episode, *Journal of Geophysical Research: Solid Earth*, 10.1029/2008JB006281.

Tait, S., C. Jaupart, and S. Vergniolle (1989), Pressure, gas content and eruption periodicity of a shallow, crystallizing magma chamber, *Earth and Planetary Science Letters*, *92*(1), 107–123, 10.1016/0012-821x(89)90025-3.

Tarantola, A., and B. Valette (1982), Generalized nonlinear inverse problems solved using the least squares criterion, 10.1029/RG020i002p00219.

Tizzani, P., M. Battaglia, R. Castaldo, A. Pepe, G. Zeni, and R. Lanari (2015), Magma and fluid migration at Yellowstone Caldera in the last three decades inferred from InSAR, leveling, and gravity measurements, *Journal of Geophysical Research-Solid Earth*, *120*(4), 2627–2647, 10.1002/2014jb011502.

Townsend, M., C. Huber, W. Degruyter, and O. Bachmann (2019), Magma chamber growth during inter-caldera periods: insights from thermo-mechanical modeling with applications to Laguna del Maule, Campi Flegrei, Santorini, and Aso, *Geo-*

chemistry, Geophysics, Geosystems, 10.1029/2018GC008103.

Trasatti, E., M. Polcari, M. Bonafede, and S. Stramondo (2015), Geodetic constraints to the source mechanism of the 2011-2013 unrest at Campi Flegrei (Italy) caldera, *Geophysical Research Letters*, 10.1002/2015GL063621.

Troise, C., G. De Natale, R. Schiavone, R. Somma, and R. Moretti (2019), The Campi Flegrei caldera unrest: Discriminating magma intrusions from hydrothermal effects and implications for possible evolution, 10.1016/j.earscirev.2018.11.007.

Vasco, D. W., C. M. Puskas, R. B. Smith, and C. M. Meertens (2007), Crustal deformation and source models of the Yellowstone volcanic field from geodetic data, *Journal of Geophysical Research: Solid Earth*, 10.1029/2006JB004641.

Waite, G. P., and R. B. Smith (2002), Seismic evidence for fluid migration accompanying subsidence of the Yellowstone caldera, *Journal of Geophysical Research: Solid Earth*, 10.1029/2001jb000586.

Walwer, D., M. Ghil, and E. Calais (2019), Oscillatory nature of the Okmok volcano's deformation, *Earth and Planetary Science Letters*, 10.1016/j.epsl.2018.10.033.

Wdowinski, S., and S. H. Hong (2015), Wetland inSAR: A review of the technique and applications, in *Remote Sensing of Wetlands: Applications and Advances*, 10.1201/b18210.

Wicks, C., W. Thatcher, and D. Dzurisin (1998), Migration of fluids beneath Yellowstone caldera inferred from satellite radar interferometry, *Science*, *282*(5388), 458–462, 10.1126/science.282.5388.458.

Wicks, C. W., W. Thatcher, D. Dzurisin, and J. Svarc (2006), Uplift, thermal unrest and magma intrusion at Yellowstone caldera, *Nature*, 10.1038/nature04507.

Wicks, C. W., D. Dzurisin, J. B. Lowenstern, and J. Svarc (2020), Magma intrusion and volatile ascent beneath Norris Geyser Basin, Yellowstone National Park, *Journal of Geophysical Research: Solid Earth*, *n/a*(n/a), e2019JB018,208, 10.1029/2019JB018208.